

1 **Observations of relative humidity effects on aerosol light**
2 **scattering in the Yangtze River Delta of China**

3
4 **Zhang Lu^{1,2}, Sun Junying^{1,3}, Shen Xiaojing¹, Zhang Yangmei¹, Che Haochi¹,**
5 **Ma Qianli⁴, Zhang Yiwen¹, Zhang Xiaoye¹, John A. Ogren⁵**

6 ¹ Key Laboratory of Atmospheric Chemistry of CMA, Institute of Atmospheric
7 Composition, Chinese Academy of Meteorological Sciences, Beijing 100081, China

8 ² College of Earth Science, University of Chinese Academy of Sciences, Beijing
9 100049, China

10 ³ State Key Laboratory of Cryospheric Sciences, Cold and Arid Region
11 Environmental and Engineering Research Institute, Chinese Academy of Sciences,
12 Lanzhou 730000, China

13 ⁴ LinAn Regional Atmosphere Background Station, LinAn 311307, China

14 ⁵ Earth System Research Laboratory, NOAA, Boulder, CO, USA

15 *Correspondence to:* J.Y. Sun (jysun@cams.cma.gov.cn)

16
17 **Abstract**

18 Scattering of solar radiation by aerosol particles is highly dependent on relative
19 humidity (RH) as hygroscopic particles take up water with increasing RH. To achieve
20 a better understanding of the effect of aerosol hygroscopic growth on light scattering
21 properties and radiative forcing, the aerosol scattering coefficients at RH in the range
22 of 40 to ~90% were measured using a humidified nephelometer system in the Yangtze
23 River Delta of China in March 2013. In addition, the aerosol size distribution and
24 chemical composition were measured. During the observation period, the mean and
25 standard deviation (SD) of enhancement factors at RH=85% for the scattering
26 coefficient ($f(85\%)$), backscattering coefficient ($f_b(85\%)$) and hemispheric backscatter
27 fraction ($f_\beta(85\%)$) were 1.58 ± 0.12 , 1.25 ± 0.07 and 0.79 ± 0.04 , respectively, i.e. aerosol
28 scattering coefficient and backscattering coefficient increased by 58 and 25% as the

29 RH increased from 40 to 85%. Meanwhile, the aerosol hemispheric backscatter
30 fraction decreased by 21%. The relative amount of organic matter (OM) or inorganics
31 in PM_{10} was found to be a main factor determining the magnitude of $f(RH)$. The
32 highest values of $f(RH)$ corresponded to the aerosols with a small fraction of OM, and
33 vice versa. The relative amount of NO_3^- in fine particles was strongly correlated with
34 $f(85\%)$, which suggests that NO_3^- played a vital role in aerosol hygroscopic growth
35 during this study. The mass fraction of nitrate also had a close relation to the curvature
36 of the humidograms; higher mass fractions of nitrate were associated with
37 humidograms that had the least curvature.. Aerosol hygroscopic growth caused a 47%
38 increase in the calculated aerosol direct radiative forcing at 85% RH, compared to the
39 forcing at 40% RH.

40 **1 Introduction**

41 Hygroscopic aerosols take up water as humidity increases (Engelhart et al.,
42 2011;Pilinis et al., 1989;Hänel, 1976;Covert et al., 1972). Aerosol water matters since
43 water can affect both the size and refractive indices of atmospheric aerosols, thereby
44 influencing the mass concentration, size distribution, and corresponding optical
45 properties (e.g., scattering coefficient, backscattering coefficient, single scattering
46 albedo, and asymmetry parameter) (Cheng et al., 2008;Randles et al., 2004;Malm et
47 al., 2003;Carrico et al., 2003). In particular, understanding the effect of relative
48 humidity on aerosol light scattering is important to better estimate the radiative
49 forcing and evaluate visibility impairment (Ackerman et al., 2004;Tang,
50 1996;Charlson et al., 1992;Covert et al., 1972). Besides, most of the ground-based
51 aerosol measurements are conducted in dry conditions to provide consistency within
52 and among networks. These measurements can differ significantly from the ambient
53 ones. Thus, the determination of enhancement factors for various optical variables are
54 of crucial importance for climate forcing calculations (Quinn et al., 1995;Pilinis et al.,
55 1995) and the comparison between remote sensing and ground based measurements
56 (Zhang et al., 2012;Wang and Martin, 2007;Zieger et al., 2012).

57 The Yangtze River Delta, one of the most populated and fastest growing regions

58 in China, has experienced extraordinary economic growth during the last two decades.
59 Amounting to 2.1% of the land area of China, this region contains ~11% of the
60 country's population and produces ~20% of China's Gross Domestic Product (GDP)
61 in 2013 (Wang et al., 2013). Concurrent with population increase and economic
62 growth are the increasing energy consumption and number of automobiles, causing
63 the Yangtze River Delta to become a significant source of gas and particulate
64 pollutants and secondary aerosol production. A 5-week field campaign was carried out
65 in the early winter of 1999 at LinAn, a background station in the Yangtze River Delta
66 (Xu et al., 2002). However, since then the physical and chemical properties of gas and
67 particulate pollutants have changed dramatically with the rapidly developing economy
68 and fast growing population, e.g. from 1999 to 2013, the sulfate mass concentration
69 decreased from 21.2 ± 1.5 to 8.1 ± 4.1 (mean \pm SD) (Qi et al., 2012; Xu et al.,
70 2008; ZEPB, 1999; ZEPB, 2013). In order to better understand the aerosol light
71 scattering properties and their dependency on relative humidity in the Yangtze River
72 Delta, both the scattering and backscattering coefficients under dry (RH<40%)
73 conditions and controlled, elevated relative humidity were measured, along with the
74 chemical composition and particle number size distribution.

75 The enhancement factors discussed in this work include scattering enhancement
76 factor $f(\text{RH}, \lambda)$, enhancement factor for backscattering coefficient $f_b(\text{RH}, \lambda)$ and
77 enhancement factor for hemispheric backscatter fraction $f_\beta(\text{RH}, \lambda)$. The impact of
78 relative humidity on the aerosol light scattering coefficient is called the scattering
79 enhancement factor $f(\text{RH}, \lambda)$, defined as

$$80 \quad f(\text{RH}, \lambda) = \sigma_{\text{sp}}(\text{RH}, \lambda) / \sigma_{\text{sp}}(\text{dry}, \lambda) \quad (1)$$

81 where $\sigma_{\text{sp}}(\text{dry}, \lambda)$ and $\sigma_{\text{sp}}(\text{RH}, \lambda)$ represent scattering coefficients at wavelength λ in dry
82 conditions and at a defined higher relative humidity, respectively.

83 Likewise, the impact of relative humidity on aerosol backscattering coefficient
84 can be described as the enhancement factor for backscattering coefficient $f_b(\text{RH}, \lambda)$:

$$85 \quad f_b(\text{RH}, \lambda) = \sigma_{\text{bsp}}(\text{RH}, \lambda) / \sigma_{\text{bsp}}(\text{dry}, \lambda) \quad (2)$$

86 where $\sigma_{\text{bsp}}(\text{dry}, \lambda)$ and $\sigma_{\text{bsp}}(\text{RH}, \lambda)$ represent backscattering coefficients at wavelength λ

87 in dry conditions and at a defined relative humidity, respectively. $f(\text{RH},\lambda)$ and $f_b(\text{RH},\lambda)$
88 are always greater than 1 if no significant restructuring is taken place after water
89 uptake (Weingartner et al., 1995).

90 Hemispheric backscatter fraction ($b=\sigma_{\text{bsp}}/\sigma_{\text{sp}}$) is closely related to the upscatter
91 fraction ($\bar{\beta}$), the fraction of incident solar radiation scattered into space (Wiscombe
92 and Grams, 1976). The impact of relative humidity on aerosol hemispheric
93 backscatter fraction can be defined as the enhancement factor for hemispheric
94 backscatter fraction $f_{\beta}(\text{RH},\lambda)$:

$$95 \quad f_{\beta}(\text{RH},\lambda) = b(\text{RH},\lambda)/b(\text{dry},\lambda) \quad (3)$$

96 where $b(\text{dry},\lambda)$ and $b(\text{RH},\lambda)$ represent hemispheric backscatter fraction at wavelength
97 λ in dry conditions and at the defined relative humidity. Thus, $f_{\beta}(\text{RH},\lambda)$ can be
98 rewritten as: $f_{\beta}(\text{RH},\lambda)=f_b(\text{RH},\lambda)/f_b(\text{dry},\lambda)$.

99 The wavelength dependence of scattering enhancement factor $f(\text{RH},\lambda)$ varies
100 with generalized aerosol types. Kotchenruther and Hobbs (1998) and Zieger et al.
101 (2010; 2011) found no pronounced wavelength dependence of $f(\text{RH},\lambda)$ for biomass
102 burning aerosols and arctic aerosols, respectively; Zieger et al. (2013) found small
103 variations (<5%) of $f(\text{RH},\lambda)$ at 450, 550 and 700 nm for several European sites;
104 Kotchenruther et al. (1999) and Magi and Hobbs (2003) reported significant
105 wavelength dependence of $f(\text{RH},\lambda)$ for urban/industrial aerosols off the east coast of
106 the United States. In this study, the wavelength dependence of enhancement factors
107 was also investigated. Except when specially mentioned, all the parameters discussed
108 in this study are based on the measurements at 550 nm wavelength only.

109

110 **2 Experimental sites and instrumentation**

111 **2.1 Site description**

112 This study was carried out during an intensive field sampling period from 1 to 31
113 March 2013 at LinAn Regional Atmosphere background station, which is a WMO
114 GAW regional station (30.3 °N, 119.73 °E, 138 m a.s.l.) located in the center of the
115 Yangtze River Delta, China (Fang et al., 2013) (as shown in Fig. 1). It is

116 approximately 11 km north of the city of LinAn, with a population of 1.5 million. The
117 site is ~50 km west of Hangzhou (capital of Zhejiang Province with a population of
118 ~8.8 million) and ~210 km southwest of Shanghai (a mega-city with a population of
119 ~20 million). LinAn station is on the top of a small hill, in an area primarily covered
120 by bamboo forests and paddy rice fields, and represents the background conditions of
121 the Yangtze River Delta. North of the station is a small village with ~200 inhabitants.
122 In addition, there is an activated charcoal factory ~1.4 km north of LinAn station that
123 uses bamboo wood as its source material (Qi et al., 2012). During the observation
124 period, the prevailing winds were northeasterly (NE) and southwesterly (SW) with an
125 average wind speed of $\sim 2.5 \text{ m s}^{-1}$ (SD 1.4 m s^{-1}). 72-hour back trajectories showed two
126 contrasting air mass origins: (1) air masses from Northern China through
127 long-distance transport and (2) air masses from southerly/southwesterly directions
128 with a much shorter transport distance.

129 **2.2 Measurement system and data processing**

130 The scattering enhancement factor $f(\text{RH})$ is defined as the ratio of aerosol
131 scattering coefficient at a given, elevated RH to that at a low RH (usually <40%).
132 Correspondingly, the humidification system, called a humidograph, included two
133 nephelometers operating in series with a humidifier between them. Sample air entered
134 the first nephelometer (reference nephelometer or DryNeph) through an aerosol dryer
135 (Shen et al., 2011; Tuch et al., 2009) to ensure the aerosol was at dry conditions (RH
136 inside DryNeph was $12.2 \pm 3.4\%$ (mean \pm SD) for the whole field campaign), then
137 passed through the humidifier, where the sample RH was regulated to a higher RH
138 that was ramped from ~40 to 90%, and finally entered the second nephelometer
139 (humidified nephelometer or WetNeph) where the scattering coefficient of humidified
140 aerosols was measured.

141 Aerosol total scattering (between 7 and 170 degrees) and backscattering
142 coefficients (between 90 and 170 degrees) were measured with an integrating
143 nephelometer (TSI Inc., Model 3563) at three wavelengths: blue (450 nm), green (550
144 nm) and red (700 nm). Data were recorded as 1-minute averages and a zero check was
145 performed automatically once per hour. The detailed characteristics of this instrument

146 has been described in many previous studies (Anderson and Ogren, 1998; Charlson et
147 al., 1969; Anderson et al., 1996).

148 The humidifier was built by the aerosol group in Global Monitoring Division,
149 Earth System Research Laboratory, National Ocean & Atmospheric Administration,
150 USA (NOAA/GMD), based on the design described in Carrico et al. (1998). It
151 consisted of 2 concentric tubes with a heater and insulation around the outer tube.
152 Sample air flowed through the inner tube, while water circulated between the inner
153 and outer tubes. The inner tube was made of porous extruded PTFE
154 (polytetrafluoroethylene) membrane, whose pore size is large enough for water
155 molecules, but too small for larger molecules such as oxygen to cross. The flux of
156 water vapor through the membrane was controlled by regulating the electric current to
157 the humidifier heater until the desired RH was attained. The humidity scan was a
158 one-hour cycle; RH was ramped from ~40 to 90% during the first half hour and in the
159 reverse direction during the last half hour.

160 Besides the scattering measurement, particle number size distribution and aerosol
161 chemistry were also measured at the station. Particle number size distributions from 3
162 nm to 10 μm were measured with a twin differential mobility particle sizer (TDMPMS)
163 (Birmili et al., 1999) and an aerodynamic particle sizer (APS, model 3321, TSI Inc.).
164 The mass concentrations of sulfate, nitrate, ammonium, organic matter (OM) and
165 chloride (aerodynamic diameter less than 1 μm) were measured with an aerosol mass
166 spectrometer (AMS, Aerodyne Inc.). The equivalent mass concentration of black
167 carbon (EBC) was measured with a multi angle absorption photometer (MAAP, model
168 5012, Thermo Scientific Inc.) at 637 nm wavelength (Müller et al., 2011); the
169 assumed mass absorption cross-section was $6.6 \text{ m}^2 \cdot \text{g}^{-1}$. Visibility was measured using
170 a near-forward scattering sensor (FD12, Vaisala). Meteorological data were provided
171 by the LinAn Regional Atmosphere Background Station.

172 All the instruments were housed in a measurement laboratory where room
173 temperature was controlled at $\sim 25 \text{ }^\circ\text{C}$. All data were reported in Beijing Time
174 (BJT=UTC+8 h) and all the scattering data were referenced at $T=0 \text{ }^\circ\text{C}$ and $P=1013.25$
175 hPa. The truncation error correction described by Anderson and Ogren (1998) was

176 applied to retrieve the final scattering and backscattering coefficients. The Ångström
177 exponent α defined as $\alpha = -\log[\sigma_{sp}(\lambda_1)/\sigma_{sp}(\lambda_2)]/\log[\lambda_1/\lambda_2]$, represents the wavelength
178 dependence of light scattering assuming a power law relationship of σ_{sp} and σ_{bsp} with
179 wavelength. In this study, scattering coefficients at 450 nm and 700 nm were used to
180 derive α . Normalization of f(RH) (Day and Malm, 2001) has been carried out to get
181 the final f(RH) scan values, i.e. f(40%) (the lowest RH in one cycle) is set to 1 and
182 used to normalize other f(RH) values in this cycle. It's worth mentioning that the
183 normalization of f(RH) (see Sect. 2.2) may underestimate f(RH) to some extent, since
184 some organics (e.g. humic acid sodium) take up water even when RH <40% (Sjogren
185 et al., 2007; Dick et al., 2000). To evaluate its impact, we calculated the raw f(40%)
186 value without the normalization. The average and standard deviation were 1.03 and
187 0.03 with a maximum of 1.08, which means this normalization may cause an
188 underestimate of 5% (an error of 3% was caused by the inconsistency of DryNeph and
189 WetNeph, see Sect. 2.4) at most. Figure 2c shows the un-normalized f(RH) value; the
190 lowest value of each cycle was around 1.03, which represents the inconsistency of
191 DryNeph and WetNeph.

192 **2.3 Inlet system**

193 An automatic regenerating adsorption aerosol dryer (Tuch et al., 2009) was used
194 to provide low RH sample air to DryNeph, TDMPS, APS, AMS and MAAP to ensure
195 comparability of measurements. The aerosol dryer was housed in a separate shelter
196 that was located on the rooftop (~ 5 m a.g.l.) of the measurement laboratory. Sample
197 air entered the shelter through a commercially available PM₁₀ impactor (PM₁₀ inlet,
198 URG Corporation) and then passed through the adsorption aerosol dryer (Tuch et al.,
199 2009) to reduce the RH to less than 30%. The dried sample passed through a 3/4-inch
200 diameter stainless tube to a manifold, which split the sample into 1/4 or 3/8-inch
201 diameter tubes that connected to the different instruments. The total sample flow
202 through the PM₁₀ impactor was kept at 16.7 lpm to ensure a 50% collection efficiency
203 at 10 μ m aerodynamic diameter (Bernier et al., 1979).

204 **2.4 Quality control**

205 Accurate performance of nephelometers and RH sensors is crucial to retrieve

206 reliable enhancement factors ($f(\text{RH},\lambda)$, $f_b(\text{RH},\lambda)$ and $f_\beta(\text{RH},\lambda)$), since they are defined
207 as the ratio of aerosol scattering coefficient/ backscattering coefficient/ hemispheric
208 backscatter fraction at a higher RH to those at a low RH (usually <40%). In addition,
209 the RH control in the WetNeph sensing volume is also critical to $f(\text{RH})$ measurement.
210 Therefore, several comparisons and calibrations have been carried out before and
211 during the experiment. Three external RH sensors (Vaisala, model HMP60) were
212 calibrated in the RH range of 11% to 80% using a Vaisala Humidity Calibrator
213 (HMK15) with four saturated salt solutions (LiCl, K_2CO_3 , NaCl, $(\text{NH}_4)_2\text{SO}_4$), and a
214 humidity/temperature transmitter (Vaisala, model HMT333), which was calibrated by
215 the National Center for Meteorological Metrology, China. The two internal
216 nephelometer RH sensors were calibrated to the external RH sensors with an
217 uncertainty of $\leq 2\%$. A good agreement of these RH sensors was achieved with a
218 discrepancy of <3%. Both nephelometers were calibrated with CO_2 (purity 99.999%)
219 and filtered air. Filtered air measurements were made automatically every hour to
220 track the instrument background. Comparison of scattering and backscattering
221 coefficients of the two nephelometers at low RH ($9.6 \pm 3.2\%$) was performed during 1
222 to 3 March, 2013. The total scattering coefficient and backscattering coefficient
223 measured by WetNeph were constantly 3% ($y=1.03x+1.60$, $R^2=1.000$) and 4%
224 ($y=1.04x+0.09$, $R^2=0.997$) higher than those obtained by DryNeph at 550 nm
225 (similarly for other wavelengths); the high consistency demonstrates that the two
226 nephelometers were operating quite steadily and the scattering/backscattering
227 coefficients measured by DryNeph can be corrected in order to make them
228 comparable to the measurements of WetNeph. The uncertainty of nephelometer
229 measurements is $\sim 10\%$ (Anderson et al, 1996), which, when combined with the
230 uncertainty of the measurements of the internal RH sensors, yields an uncertainty for
231 $f(85\%)$ of $\sim 20\%$. This overall uncertainty could be lower for less hygroscopic
232 particles or lower RHs.

233 The RH at the outlet of WetNeph was regulated via a feedback system using the
234 Vaisala RH signal, a PID controller and a heater. The humidifier set point was stepped
235 from low to high RH and back to low RH every hour with the set point changing

236 every one or two minutes. Figure 2 is an example of our data showing the RH control
237 and corresponding scattering measurements. As can be seen from Fig. 2, good RH
238 control was achieved regardless of the magnitude of the scattering coefficient.

239 During the drying and humidifying process, thermophoresis, coagulation,
240 evaporation, and irreversible chemical reactions can alter the particles from the
241 original ones. A variety of measures were taken to minimize changes to the particles:
242 the transport path was made as short and straight as possible, particle-free air was
243 diluted to the aerosol stream to reduce coagulation, and higher heater temperatures
244 were avoided to reduce evaporation of semi-volatile compounds like weak organic
245 acids and nitrates. The nephelometers were operated at a constant flow of 20 lpm,
246 comprised of 9 lpm sample air and 11 lpm particle-free air (dilution flow). The total
247 flowrate through the nephelometer was controlled by a mass flow controller. The
248 dilution flow was regulated by a needle valve and measured with a mass flowmeter.
249 The sample and dilution flow have been calibrated with a Gilibrator bubble flowmeter
250 before the experiment. Filtered air tests were also conducted to make sure that all the
251 instruments were in good condition and that there were no leaks in the system.

252

253 **3 Results and discussion**

254 **3.1 Overview**

255 Figure 3 shows the time series of the measured and derived aerosol variables
256 during March 2013, as well as the ambient RH and visibility. The scattering
257 enhancement factor $f(85\%)$ ranged from 1.29 to 1.86 (Fig. 3a) with an average of 1.58
258 (Table 1) for the whole campaign. During 4-9 March, when LinAn was dominated by
259 air masses from the south under clear sky, $f(85\%)$ stayed at a low value of 1.42
260 (± 0.05). In March, the hourly averaged aerosol scattering coefficient, measured under
261 dry conditions (Fig. 3c), varied from 21 to 1067 Mm^{-1} , and the maximum occurred on
262 16 March, when a severe haze occurred. The mean value and standard deviation of the
263 hourly averaged aerosol scattering coefficient was 223 Mm^{-1} (140 Mm^{-1}). Visibility
264 (Fig. 3b) varied from 0.1 km to 23.7 km at ambient conditions with a mean value of
265 6.2 km. The lowest visibilities were observed on 23 and 24 March, when the station

266 was in clouds. From 15 to 16 March, visibility declined to 4.4 km with the
267 accumulation of pollutants in the atmosphere, which was a severe haze episode (as
268 mentioned above). An air mass from Northwest China with high dust levels arrived at
269 LinAn on 10 March, with an abrupt increase of the aerosol scattering coefficient (Fig.
270 3c) and a sharp decline of Ångström exponent (Fig. 3d).

271 Based on nephelometer measurements, the enhancement factors for scattering
272 coefficient $f(\text{RH})$, backscattering coefficient $f_b(\text{RH})$ and hemispheric backscatter
273 fraction $f_\beta(\text{RH})$ were determined using Eq. (1), (2) and (3), respectively. Their values
274 at different RHs (50, 60, 70, 80 and 85%) were obtained using linear interpolation
275 from the half-hourly humidogram data (Table 1). The enhancement factors $f(\text{RH})$ and
276 $f_b(\text{RH})$ increased as the RH increased, but $f_b(\text{RH})$ increased much more slowly than
277 $f(\text{RH})$. The $f(85\%)$ and $f_b(85\%)$ were 1.58 and 1.25, respectively, suggesting that the
278 scattering coefficient and backscattering coefficient at 85% RH were 58 and 25%
279 higher than those in dry conditions due to aerosol water uptake. The $f_\beta(\text{RH})$ decreased
280 with increasing RH, i.e. hemispheric backscatter fraction becomes smaller with the
281 increase of RH and the fraction of radiation that would be backscattered into space
282 was reduced. The $f_\beta(\text{RH})$ decreased $\sim 21\%$ as the RH increased from 40 to 85%. All
283 these parameters are of crucial importance in evaluating the aerosol radiative forcing.

284 Generally, the scattering enhancement factor ($f(80\%)=1.44$) is much lower than
285 the result ($f(80\%)=1.7-2.1$) obtained by Xu et al. (2002) for LinAn in 1999. This value
286 is also lower than the results obtained by Carrico during ACE-1 (Carrico et al., 1998)
287 and ACE-Asia (Carrico et al., 2003), the values obtained by Zieger et al. (2013) in
288 several European sites and the Arctic, as well as the values reported at several sites in
289 the U.S. (Malm et al., 2005;Malm et al., 2003;Malm and Day, 2001;Day and Malm,
290 2001;Malm and Day, 2000). However, the difference between measured $f(\text{RH})$ in this
291 study and previous studies performed in China (Yan et al., 2009;Pan et al., 2009;Liu
292 et al., 2009;Cheng et al., 2008) are much smaller. The enhancement factors for
293 backscattering coefficient and hemispheric backscatter fraction ($f_b(85\%)$ and $f_\beta(85\%)$)
294 were 1.25(0.07) and 0.79(0.04), respectively, similar to the results
295 ($f_b(82\%)=1.22\pm 0.06$ and $f_\beta(82\%) =0.83$) obtained by Carrico at Sagres, Portugal

296 during ACE-2 (Carrico et al., 2000) and the results ($f_b(82\%)=1.27$ and $f_\beta(82\%) =0.75$)
297 obtained by Carrico et al. (2003) during the dust-dominant period in ACE-Asia.

298 **3.2 Aerosol chemical properties**

299 The submicron mass concentrations of sulfate, nitrate, ammonium, chloride and
300 organic matter (OM) measured by AMS, plus EBC in PM_{10} measured by MAAP, are
301 summarized in Table 2. The mass concentration of OM is the largest, while the mass
302 concentration of chloride is the smallest, in accord with previous studies in LinAn
303 (Meng et al., 2012; Yan et al., 2005). The mean mass concentrations of nitrate and
304 sulfate were $9.8 \pm 12.1 \mu\text{g}\cdot\text{m}^{-3}$ and $8.1 \pm 4.1 \mu\text{g}\cdot\text{m}^{-3}$ in this study, similar to the values
305 ($9.4 \pm 7.1 \mu\text{g}\cdot\text{m}^{-3}$ for nitrate and $8.6 \pm 3.7 \mu\text{g}\cdot\text{m}^{-3}$ for sulfate in $PM_{2.5}$) at LinAn in
306 summer, 2010 (Meng et al., 2012).

307 Aerosol acidity is a key parameter affecting aerosol hygroscopic growth. It is
308 usually examined by comparing the NH_4^+ mass concentration and the amount needed
309 to fully neutralize sulfate, nitrate and chloride ions ($\text{NH}_4^+_{\text{predicted}}$) (Sun et al., 2010):

$$310 \quad \text{NH}_4^+_{\text{predicted}} = 18 \times (2 * \text{SO}_4^{2-}/96 + \text{NO}_3^-/62 + \text{Cl}^-/35.5) \quad (4)$$

311 Figure 4 illustrates the relationship of measured NH_4^+ and predicted NH_4^+ . As
312 shown in Fig. 4, the regression slope is close to 1, which implies that there was
313 sufficient NH_3 in the atmosphere to neutralize H_2SO_4 , HNO_3 and HCl , and that the
314 PM_1 aerosol at LinAn was bulk neutralized during the measurement period. Therefore,
315 the dominant chemical form of sulfate aerosol is ammonium sulfate (AS) rather than
316 acidic sulfate (H_2SO_4 or NH_4HSO_4) and the nitrate existed in the form of NH_4NO_3
317 (AN). By calculating Pearson's correlation coefficient among 5 different chemical
318 species, it was found that NH_4^+ and NO_3^- are strongly correlated with $r=0.93$; NH_4^+
319 and SO_4^{2-} , Cl^- are highly related with r equal to 0.77 and 0.74 respectively, which
320 also implies the main form of inorganics would be NH_4NO_3 , $(\text{NH}_4)_2\text{SO}_4$ and NH_4Cl .
321 However, the average mass concentration of chloride was very low (see Table 2) at
322 LinAn, and NH_4NO_3 and $(\text{NH}_4)_2\text{SO}_4$ were the dominant water-soluble ionic species,
323 consistent with previous results at LinAn based on filter chemical measurements
324 (Meng et al., 2012).

325 **3.3 Wavelength dependence of the scattering enhancement factor f(85%)**

326 The wavelength dependence of the scattering enhancement factor is needed to
327 estimate the aerosol radiative forcing since solar radiation at Earth's surface depends
328 on wavelength. The histogram for $f(85\%, 550 \text{ nm})$ is shown in Fig. 5. Overlaid on the
329 histogram for $f(85\%, 550 \text{ nm})$ (Fig. 5) are Gaussian curves based on the statistics for
330 $f(85\%)$ at each wavelength. No apparent shift of mean $f(85\%)$ is seen for the 550 nm
331 and 700 nm wavelength pair (see Fig. 5); while the mean $f(85\%, 450 \text{ nm})$ is ~6%
332 lower than that at 550 nm with a smaller standard deviation (see Fig. 5). For higher
333 values (90th and 70th percentile values in Table 3), a slight wavelength dependence of
334 $f(\text{RH})$ can be observed, i.e. the $f(\text{RH})$ increases with the increase of wavelength.
335 However, the differences are mostly under 10% and therefore the discussion is
336 focused on 550 nm wavelength in this study. Similar results were obtained by Zieger
337 at a regional continental research site at Melpitz, Germany (Zieger et al., 2014).

338 **3.4 Classification of various observation episodes**

339 Based on wind direction, back trajectory analysis and weather phenomena, the
340 observation period can be classified into three main sectors: a northerly-polluted
341 period (influenced by long-distance transport from northern China), a locally-polluted
342 period, and a dust-influenced episode. Air mass back trajectories over 72 hours at
343 300m a.g.l. arrival height were calculated using the Trajectory Statistics (TrajStat)
344 model (Wang et al., 2009) with 6-hourly archived meteorological data provided by the
345 US National Centers for Environmental Prediction (NCEP). The characteristics of
346 these three periods are as follows:

- 347 1. Periods when the wind direction is between 120° and 270° are labelled as
348 "locally-polluted periods". During these periods, pollutants mostly came from
349 Anhui province, Jiangxi province and the southern region of Zhejiang province as
350 well as LinAn (green line in Fig. 6). Economy in these areas is mainly made up of
351 manufacturing, tourism and agriculture.
- 352 2. Periods when the wind direction was greater than 270° or less than 120° are
353 described as "northerly-polluted periods". Back trajectories indicate that most of
354 the air masses came from northern China and passed over heavily polluted areas

355 such as the Beijing-Tianjin-Tangshan economic region and the Yangtze River
356 Delta during long-distance transport (red line in Fig. 6).

357 3. A heavy dust event occurred at LinAn on 10 March (approximately from 02:00
358 BJT) according to satellite information (<https://earthdata.nasa.gov/labs/worldview/>)
359 and meteorology information (provided by China Meteorological Administration,
360 CMA). The 72 h back trajectory shows the air masses tracked from Mongolia and
361 passed over Inner Mongolia (blue line in Fig. 6).

362 **3.4.1 Locally-polluted periods**

363 During the periods of 4-9, 15-20 and 26-30 March, 2013, aerosols were mainly
364 from local pollution sources in Zhejiang and/or nearby provinces. The mean $f(80\%)$
365 and $f(85\%)$ were 1.36 and 1.52 (as shown in Table 4), ~10 and 8% lower than those in
366 northerly-polluted periods.

367 The enhancement factor for scattering and backscattering coefficients at 80%
368 during locally-polluted periods was 1.36 and 1.15, respectively, similar to the values
369 ($f(82.5\%)=1.4-1.5$) and ($f_{\beta}(82.5\%)=1.1-1.2$) obtained by Koloutsou-Vakakis et al.
370 (2001) at a continental U.S. site (Bondville, Illinois, US). The measured dry scattering
371 coefficient was 217 Mm^{-1} , ~15% lower than that of the northerly-polluted period (251
372 Mm^{-1}). The averaged mass percentages of sulfate, nitrate, ammonium, OM, chloride
373 and EBC were 17.6, 16.1, 13.0, 42.2, 1.5 and 9.6%, respectively (Fig. 6a); for this and
374 subsequent calculations of mass percentages, the denominator is the sum of the mass
375 concentrations of sulfate, nitrate, ammonium, OM, chloride and EBC. Compared to
376 the northerly-polluted period, the mass percentage of OM was ~27% higher during
377 the locally-polluted period, while the mass percentage of nitrate was ~33% lower.
378 Although the $\text{OM}/(\text{OM} + \text{SO}_4^{2-})$ ratios during locally-polluted (~0.70) and
379 northerly-polluted periods (~0.67) were similar, the $\text{OM}/(\text{OM} + \text{NO}_3^- + \text{SO}_4^{2-})$ ratio
380 during the locally-polluted periods (~0.56) was 24% higher than that during the
381 northerly-polluted periods (~0.45), which may partly explain the lower $f(\text{RH})$ during
382 locally-polluted episodes (as discussed later in Sect. 3.5).

383 **3.4.2 Northerly-polluted periods**

384 The air masses reaching LinAn during the periods March 1-3, 11-15, 20-26 and

385 30-31 (dust episode excluded) mainly came from northern China through
386 long-distance transport. The mean $f(80\%)$ and $f(85\%)$ were 1.50 and 1.64 ,
387 respectively (as shown in Table 4).

388 The value ($f(80\%)=1.50$) is similar to the previous results ($f(80\%)=1.48$)
389 obtained by Yan et al. (2009) for periods influenced by the urban plume from Beijing,
390 ($f(80\%)=1.46\pm 0.10$) reported by Carrico et al. (2000) for anthropogenic aerosols in
391 Europe during the 2nd Aerosol Characterization Experiment (ACE-2) campaign, and
392 ($f(80\%)=1.55-1.59$) indicated by Pan et al. (2009) for a rural site (Xin'an) near
393 Beijing city during pollution periods. However, the measured $f(80\%)$ was much lower
394 than ($f(80\%)=2.0-2.43$) during a pollution episode reported by Kim et al. (2006) at the
395 Gosan regional background site, 720 km northeast of LinAn and results
396 ($f(82\%)=2.24\pm 0.20$) obtained by Carrico et al. (2003) in ACE-Asia for polluted air
397 masses measured over the ocean. The $f(RH)$ of continental air masses transported
398 over the ocean was higher than that over the continent, and the possible mechanisms
399 for that increase might include coagulation with sea-salt particles and the oxidation of
400 SO_2 and VOCs (volatile organic compounds) leading to an increase in aerosol
401 hygroscopicity.

402 **3.4.3 Dust-influenced episode**

403 During a severe cold air outbreak, a strong dust event struck northern China on 8
404 and 9 March, 2013. The affected area covered about 2.8 million square kilometers,
405 about 10% of which suffered from dust storms or strong sandstorms. This event was
406 considered to be the largest and strongest dust event to hit China in 2013. During this
407 event, suspended dust appeared in most of northwestern China, northern China, north
408 and west Huanghuai region and west Liaoning province, while west-central Inner
409 Mongolia, west Gansu, northern Shanxi, and several parts of Xinjiang experienced a
410 sandstorm. Along with the extreme dust event, there was a dramatic increase in PM_{10} ,
411 for example, the PM_{10} in Yulin, Shanxi even reached $10,000 \mu g \cdot m^{-3}$ (Wang et al.,
412 2013;Zhang and Sun, 2013).

413 At 2 a.m. on March 10, the wind direction changed abruptly to northerly (see Fig.
414 8d) and the scattering coefficient increased abruptly from $\sim 200 Mm^{-1}$ to $> 600 Mm^{-1}$

415 (Fig. 7b). PM_{10} mass concentrations at LinAn increased rapidly from $100 \mu\text{g}\cdot\text{m}^{-3}$ to
416 $637 \mu\text{g}\cdot\text{m}^{-3}$, while the $PM_{2.5}$ mass concentration was only $190 \mu\text{g}\cdot\text{m}^{-3}$, accounting for
417 30% of PM_{10} . The Ångström exponent decreased from 1.2 to 0.8 (see Fig. 7c). All
418 these phenomena implied the arrival of cold front from northern China enriched in
419 coarse mode particles. The mass percentage of nitrate increased significantly and
420 reached its peak ($\sim 26\%$) at 3 a.m.; meanwhile, the mass percentage of OM decreased
421 sharply from 2 a.m. to 3 a.m. (see Fig. 7e). Correspondingly, the scattering
422 enhancement factor $f(85\%)$ reached 1.52 at 3 a.m. (see Fig. 7a), an increase of $\sim 16\%$
423 compared with that before the dust arrival. The most dust-dominated period, from 7
424 a.m. to 1 p.m., when the Ångström exponent was below 0.5 (Fig. 7c) and scattering
425 coefficients at 450 nm, 550 nm and 700 nm (Fig. 7b) were nearly equal, the scattering
426 enhancement factor $f(85\%)$ was ~ 1.46 . This value is much higher than the results
427 ($f(80\%)=1.20$) reported by Pan et al. (2009) in rural Beijing, ($f(82.5\%)=1.18$)
428 obtained by Carrico et al. (2003) in East Asia (ACE-Asia) during a dust episode,
429 ($f(80\%)=1.20$) reported by Fierz-Schmidhauser et al. (2010) at a high alpine site
430 (Jungfrauoch, 3580m a.s.l.) in Switzerland during a strong Saharan dust event, and
431 ($f(80\%)=1.0-1.1$) measured by Li-Jones et al. (1998) in South America during an
432 investigation of long-range transported Saharan dust. Meanwhile it is much lower
433 than the value ($f(85\%)=1.73-2.20$) obtained by Kim et al. (2006) in Gosan (South
434 Korea) during a dust-dominated period. According to Tobo et al. (2010), Ca-rich
435 particles can react with gaseous HNO_3 to form $\text{Ca}(\text{NO}_3)_2$, thus the liquid
436 cloud-nucleating ability would be enhanced. Similar results have also reported that
437 aerosol hygroscopicity would be largely enhanced if coarse mode Ca-rich particles
438 combined with nitrate (Shi et al., 2008; Sullivan et al., 2009). Thus, it is speculated
439 that the relatively high $f(\text{RH})$ may have resulted from the reactions of coarse mode
440 particles with inorganics (very likely to be nitrate) during long-range transport.

441 **3.5 The relationship of scattering enhancement factor with chemical composition**

442 Scattering enhancement factor $f(85\%)$ versus organic mass fraction and inorganic
443 mass fraction are shown in Fig. 8. The total mass concentration was calculated as the
444 sum of mass concentrations of sulfate, nitrate, ammonium, chloride and organic

445 measured by AMS and EBC measured by MAAP. The organic and inorganic mass
446 fractions were calculated by dividing the mass concentration of organics (measured
447 by AMS) and inorganics (the sum of sulfate, nitrate, ammonium and chloride
448 measured by AMS) by the total mass concentration, respectively. The bivariate linear
449 regression was applied with the uncertainty of $f(85\%, 550\text{nm})$ which was discussed in
450 Sect. 2.4 and the standard deviation of chemical compositions. The bivariate linear
451 regressions (Fig. 8) clearly show anti-correlation of $f(85\%, 550\text{nm})$ with the organic
452 fraction and strong positive correlation of $f(85\%, 550\text{nm})$ to the inorganic fraction.
453 This implies that chemical composition plays a vital role in aerosol hygroscopic
454 properties. The absolute values of both slopes (1.2 for $f(85\%)$ vs. organic mass
455 fraction and 0.96 for $f(85\%)$ vs. inorganic mass fraction) were much lower than those
456 (3.1 and 2.2, respectively) measured at Melpitz, Germany (Zieger et al., 2014). This
457 may partly be due to the higher organic (or lower inorganic) content at LinAn.
458 Comparing Fig. 8 (a)(b) with (c)(d), a stronger association of increasing nitrate with
459 increasing $f(85\%)$ was observed. The role nitrate plays in aerosol hygroscopic
460 properties will be discussed in the following paragraph.

461 $f(\text{RH})$ in Fig. 9 was expressed in terms of γ so as to be applied to a broader RH
462 range (Doherty et al., 2005; Quinn et al., 2005): $\gamma = \ln f(\text{RH}) / \ln((100 - \text{RH}_{\text{ref}}) / (100 - \text{RH}))$.
463 Here γ was based on $\text{RH}_{\text{ref}} = 40\%$ and $\text{RH} = 85\%$. The relative amount of OM and
464 inorganics can be expressed as $F_o = C_c / (C_c + C_i)$, where C_c and C_i are the mass
465 concentrations of OM and inorganics, respectively. Figure 9 shows γ versus F_o where
466 C_i was the mass concentrations of SO_4^{2-} , NO_3^- and $\text{NO}_3^- + \text{SO}_4^{2-}$ in Fig. 9a, Fig. 9b
467 and Fig. 9c, respectively. For all three scatter plots, there is a trend of decreasing γ
468 with increasing F_o . However, unlike the results of Quinn et al. (2005), Malm et al.
469 (2005), Pan et al. (2009) and Yan et al. (2009), γ and F_o ($\text{OM} / (\text{OM} + \text{SO}_4^{2-})$) (Fig. 9a)
470 were uncorrelated ($R^2 = 0.14$), while γ and F_o ($\text{OM} / (\text{OM} + \text{NO}_3^-)$) (Fig. 9b) and γ and F_o
471 ($\text{OM} / (\text{OM} + \text{SO}_4^{2-} + \text{NO}_3^-)$) (Fig. 9c) were more strongly correlated (R^2 of 0.56 and 0.68,
472 respectively). This result implies that NO_3^- played a stronger role in determining
473 aerosol hygroscopic growth than SO_4^{2-} during this study. This increasing importance
474 of nitrate corresponds to many recent studies in Shanghai (a mega city in Yangtze

475 River Delta) (Shi et al., 2014) and Beijing (Sun et al., 2012). This may partly result
476 from increasing availability of NH_3 to form NH_4NO_3 (Morgan et al., 2010) due to the
477 decrease of SO_2 . The Chinese government has put an emphasis on the control of SO_2
478 emissions in recent years, and desulfurization technology has been installed at
479 coal-fired power units as well as certain steel and cement production facilities. As a
480 result, the annual average concentration of SO_2 decreased significantly from 56 to 19
481 $\mu\text{g m}^{-3}$ at LinAn from 2006 to 2012 (ZEPB, 2012; 2006).

482 The molar ratio of particulate SO_4^{2-} to total sulfur (SO_4^{2-} + gas phase SO_2) was
483 used as an indicator of the relative age of aerosols (Quinn et al., 2005). For relatively
484 younger aerosols, there is insufficient time for the conversion of SO_2 to SO_4^{2-} via gas
485 and aqueous phase oxidation process and therefore the $\text{SO}_4^{2-}/(\text{SO}_4^{2-} + \text{SO}_2)$ molar ratio
486 is low. As aerosol ages, more SO_2 is converted to SO_4^{2-} and thus the ratio increases.
487 To illustrate the effects of this ratio and scattering coefficient on γ , Fig. 10 shows γ
488 versus $\text{Fo} = \text{OM}/(\text{OM} + \text{SO}_4^{2-} + \text{NO}_3^-)$ colored by the $\text{SO}_4^{2-}/(\text{SO}_4^{2-} + \text{SO}_2)$ molar ratio (Fig.
489 10a) and $\log_{10}(\sigma_{\text{sp}})$ (Fig. 10b). The highest values of γ (or $f(\text{RH})$) corresponded to
490 more aged aerosols with a low OM content, while the lowest values corresponded to
491 younger aerosols with a higher OM content, consistent with the result of Quinn et al.
492 (2005). For aerosols with relatively low scattering coefficients, the value of $f(\text{RH})$ was
493 usually low with a large variation (dots with cooler colors in Fig. 10b), while aerosols
494 with high scattering coefficients had values of $f(\text{RH})$ that were relatively high with a
495 small variation (dots with warm colors in Fig. 10b).

496 **3.6 Parameterization of scattering enhancement factor $f(\text{RH})$**

497 The scattering enhancement factor $f(\text{RH})$ can be parameterized with empirical
498 equations (Kotchenruther and Hobbs, 1998; Kotchenruther et al., 1999; Gassó et al.,
499 2000; Carrico et al., 2003; Liu et al., 2008; Pan et al., 2009; Zieger et al., 2010; Zieger
500 et al., 2014). Humidograms from LinAn were fitted with two empirical equations and
501 the fitting results are shown below.

502 **3.6.1 Parameterization with equation $f(\text{RH}) = c (1 - \text{RH})^{-g}$**

503 Kasten (1969) proposed an empirical equation $f(\text{RH}) = c (1 - \text{RH})^{-g}$ to describe how
504 $f(\text{RH})$ varies with RH , which has been used in previous reports e.g. by Kotchenruther

505 and Hobbs (1998), Gass ó et al. (2000), Carrico et al. (2003) and Zieger et al. (2010,
506 2014). Table 5 shows the fitting results from the current work and previous studies.
507 Larger $f(\text{RH})$ values are associated with larger values of “c” and “g”. In this work, “g”
508 was much lower than that in most of the other studies, although it was similar to the
509 result of Gass ó et al. (2000) during a dust episode. The similarity results from the low
510 scattering enhancement factor (e.g. $f(80\%)=1.44\pm 0.12$) at LinAn, which was similar
511 to the value ($f(80\%)=1.33\pm 0.07$) obtained by Gass ó et al. (2000) for a dust event. The
512 $f(\text{RH})$ in other studies was much higher than that at LinAn, ranging from 2.04
513 (polluted marine aerosols in Gass ó et al. (2000)) to 3.77 (arctic aerosols in Zieger et al.
514 (2010)), therefore their parameter “g” was much higher.

515 **3.6.2 Parameterization with equation $f(\text{RH})=1+a \text{RH}^b$**

516 The $f(\text{RH})$ obtained at LinAn station can also be well described by the following
517 equation, which was proposed by Kotchenruther and Hobbs (1998):

$$518 \quad f(\text{RH})=1+a \text{RH}^b \quad (5)$$

519 where “a” is positive and “b” is greater than 1. This function is convex, and has been
520 used in many previous studies (Pan et al., 2009; Carrico et al., 2003; Kotchenruther et
521 al., 1999; Kotchenruther and Hobbs, 1998) to describe monotonic growth.
522 Theoretically, parameter “a” determines the largest value $f(100\%)$ can reach, and
523 parameter “b” dominates the curvature of the function. The smaller “b” is, the smaller
524 the curvature of humidogram will be; if “b” equals to 1, then $f(\text{RH})=1+a\cdot\text{RH}$. The
525 parameters “a” and “b” from our study and previous results for different aerosol types
526 are listed in Table 6. Taking the locally-polluted episode as an example, although
527 parameter “a” is slightly larger (~3%) than in the northerly-polluted episode,
528 parameter “b” is ~40% larger; as a result the $f(85\%)$ during locally-polluted periods is
529 smaller. Parameter “b” is greatest in the locally-polluted episode and smallest in the
530 northerly-polluted period, i.e. the curvature of RH- $f(\text{RH})$ line is largest during the
531 locally-polluted episode, then is the dust episode, and the northerly-polluted period
532 shows the least curvature. These variations in curvature are associated with the mass
533 percentages of nitrate, as will be discussed later (c.f. Fig. 6).

534 **3.6.3 Steepness of humidograms**

535 For all the humidograms measured at LinAn, $f(\text{RH})$ increases continuously and
536 monotonically. However, the curvatures of the humidograms can be different (Fig. 11);
537 some increase with a nearly constant rate and the humidogram curve is almost straight,
538 while some increase slowly at first and then increase more steeply at relatively higher
539 RH, thus the curvature of the humidogram is larger. In order to describe the growth
540 pattern quantitatively, a steepness index η is defined based on the fitting curve:

$$541 \quad \eta = f'(80\%) / f'(60\%) - 1 = (4/3)^{b-1} - 1 \quad (6)$$

542 where $f'(60\%)$ and $f'(80\%)$ represent the derivatives of the fitting curve at 60% and 80%
543 RH, respectively. η is a nonnegative number. Zieger et al. (2010) has defined an index
544 describing the magnitude of deliquescence transitions based on fitting equation
545 $f(\text{RH}) = (1 - \text{RH})^{-g}$ (see Sect. 3.6.1), while the steepness index η proposed in this study
546 provided a way of quantitatively describing the steepness of humidograms that are
547 well described by the equation $f(\text{RH}) = 1 + a \text{RH}^b$. The larger η is, the greater the
548 curvature. As is shown in Fig. 11a, for a large η , the $f'(60\%)$ is very small, meaning
549 that aerosol scattering coefficient barely increases ($f(\text{RH}) \approx 1$) under low RH (usually
550 $< 70\%$). Once reaching larger RH ($\sim 70\%$), $f(\text{RH})$ begins to increase. However, for a
551 small η (Fig. 11b), the difference of the derivatives at 60% and 80% RH was small,
552 meaning the curvature of humidogram is much smaller.

553 A scatter plot of η and the mass percentage of nitrate is shown in Fig. 12, colored
554 by the mass percentage of sulfate. As can be seen, η is negatively correlated with the
555 mass percentage of nitrate. When the mass percentage of nitrate is below $\sim 18\%$, η
556 decreases strongly as nitrate percentages increase, which means that the humidogram
557 line becomes straighter and the difference of the derivatives at lower and higher RHs
558 becomes smaller. For a mass percentage of nitrate higher than 18% (correspondingly,
559 a lower sulfate mass percentage), η is ~ 1.1 , meaning the humidogram line is almost
560 straight (as shown in Fig. 11b) and aerosol scattering coefficient experiences a
561 continuous and smooth growth at almost the same rate with RH.

562 **3.7 Sensitivity of the direct radiative forcing of different aerosols to $f(\text{RH})$**

563 Direct radiative forcing of aerosols is quite sensitive to changes of relative
564 humidity. The impact of relative humidity on globally-averaged, direct radiative

565 forcing can be obtained by the following expression (Chylek and Wong, 1995):

$$566 \quad \Delta F_R(\text{RH}) = -[S_0/4][T_a^2(1 - A_c)][2(1 - R_s)^2\bar{\beta}(\text{RH})M\alpha_s f(\text{RH}) - 4R_s M\alpha_a] \quad (7)$$

567 where S_0 is the solar constant, T_a is the transmittance of the atmosphere above the
568 aerosol layer, A_c is the fractional cloud amount, R_s is the albedo of the underlying
569 surface, $\bar{\beta}(\text{RH})$ is the solar radiation scattered back to space at defined RH, $f(\text{RH})$ is
570 the scattering enhancement factor, M is the column burden of aerosol (in g m^{-2}), α_s is
571 the mass scattering efficiency, and α_a is the mass absorption efficiency.

572 In order to estimate the sensitivity of the forcing to RH for various aerosol types
573 at LinAn (locally-polluted, northerly-polluted and dust-influenced aerosols), the ratio
574 of direct aerosol radiative forcing ΔF_R at a defined RH to that at dry condition was
575 calculated:

$$\frac{\Delta F_R(\text{RH})}{\Delta F_R(\text{dry})} = \frac{(1 - R_s)^2\bar{\beta}(\text{RH})\alpha_s f(\text{RH}) - 2R_s\alpha_a}{(1 - R_s)^2\bar{\beta}(\text{dry})\alpha_s f(\text{dry}) - 2R_s\alpha_a} \quad (8)$$

576 Parameters used in Eq. (8) were $R_s=0.15$, and $\alpha_a=0.3 \text{ m}^2\text{g}^{-1}$ (Wang et al., 2012; Hand
577 and Malm, 2007). The mass scattering efficiency α_s is $2.76 \text{ m}^2\text{g}^{-1}$, which is derived
578 from the slope of a linear regression of the measured scattering coefficients and the
579 calculated PM_{10} mass concentrations based on TDMPS and APS measurement (Fig.
580 13); the high mass scattering efficiency is explained by the high ratio of PM_1 to PM_{10}
581 mass at this site (average 0.81). The average upscatter fraction $\bar{\beta}$ was calculated as
582 $\bar{\beta}=0.0817+1.8495b-2.9682b^2$ (Delene and Ogren, 2002). The sensitivity of direct
583 radiative forcing to RH for various aerosol types is shown in Fig. 14. As is shown in
584 the figure, the variation of $\Delta F_R(\text{RH})/\Delta F_R(\text{dry})$ with RH corresponds to the variation of
585 humidograms. The $f(\text{RH})$ values were the largest during the northerly-polluted period,
586 correspondingly, the effect of RH on aerosol radiative forcing during this period was
587 the largest. The same was true for the locally-polluted period and the dust-influenced
588 period. Since b decreases with increasing RH, this correspondence also demonstrates
589 the vital role $f(\text{RH})$ plays in direct forcing enhancement. At 85% RH, the average ratio
590 was 1.47, i.e. the direct radiative forcing increased by 47% owing to the aerosol
591 hygroscopicity.

592 Table 7 shows the mean influence of aerosol hygroscopicity on direct radiative

593 forcing in March at LinAn. The ratios $\Delta F_R(\text{RH}_{\text{amb}})/\Delta F_R(\text{dry})$ for locally-polluted,
594 northerly-polluted and dust-influenced aerosols were calculated using the ambient
595 average RH ($\text{RH}_{\text{amb}}=67\%$) in March at LinAn. The variables $f(\text{RH}_{\text{amb}})$, $b(\text{RH}_{\text{amb}})$,
596 $\bar{\beta}(\text{RH}_{\text{amb}})$ and $\Delta F_R(\text{RH}_{\text{amb}})/\Delta F_R(\text{dry})$ were the averages of the linear interpolation
597 results of $f(\text{RH})$, $b(\text{RH})$, $\bar{\beta}(\text{RH})$ and $\Delta F_R(\text{RH})/\Delta F_R(\text{dry})$ to 67% RH. The
598 $\Delta F_R(\text{RH}_{\text{amb}})/\Delta F_R(\text{dry})$ ratios were 1.118, 1.195 and 1.105, respectively (see Table 7).
599 That is to say, on average, the direct radiative forcing of locally-polluted,
600 northerly-polluted and dust-influenced aerosols increased by 11.8, 19.5 and 10.5% in
601 March at LinAn.

602

603 **4 Conclusions**

604 The influence of aerosol water uptake on aerosol light scattering properties and
605 direct radiative forcing have been investigated at LinAn, a regional atmospheric
606 background station in the Yangtze River Delta, China, using a scattering enhancement
607 factor measurement system, together with chemical composition and size distribution
608 information. The average enhancement factors and mean standard deviations at 85%
609 RH for scattering coefficient, backscattering coefficient and hemispheric backscatter
610 fraction ($f(85\%)$, $f_b(85\%)$ and $f_{\beta}(85\%)$) were 1.58(0.12), 1.25(0.07) and 0.79(0.04),
611 respectively. A slight wavelength dependence of $f(85\%)$ was observed at higher $f(\text{RH})$
612 values. Generally, the highest values of $f(\text{RH})$ corresponded to aged aerosols with a
613 small fraction of OM, while the lowest values corresponded to younger aerosols with
614 a larger fraction of OM. $f(\text{RH})$ of aerosols with relatively low scattering coefficients
615 was usually low with a large variation; while $f(\text{RH})$ of aerosols with high scattering
616 coefficients was relatively high with a small variation. Nitrate was found to play an
617 important role in determining the magnitude of $f(\text{RH})$ at LinAn.

618 Humidograms measured at LinAn can be well described by two equations:
619 $f(\text{RH})=c(1-\text{RH})^{-d}$ and $f(\text{RH})=1+a\cdot\text{RH}^b$. Further investigation shows the shape of the
620 humidogram is closely related to the mass percentage of nitrate. A steepness index η
621 has been defined to quantitatively determine the steepness of the humidograms. The
622 least curvature of the humidograms (smallest η) was associated with the highest

623 nitrate mass fractions (and lowest sulfate fractions). In March, the average relative
624 humidity (RH_{amb}) was 67%. Consequently, the direct radiative forcing of
625 locally-polluted, northerly-polluted and dust-influenced aerosols increased by 11.8,
626 19.5 and 10.5%, respectively due to aerosol uptake water in March at LinAn. At 85%
627 RH, the direct radiative forcing increased by as much as 47% due to aerosol
628 hygroscopicity. In conclusion, water plays an important role in aerosol scattering
629 properties as well as the radiative forcing, and careful attention to humidity effects is
630 required when comparing remote sensing and in-situ measurements or calculating the
631 climate forcing.

632

633

634 **Acknowledgments:** This work was supported by National Basic Research Program of
635 China (2011CB403401), the National Natural Science Foundation of China
636 (41475118, 41175113), China International Science and Technology Cooperation
637 Project (2009DFA22800), CAMS Basis Research Project (2013Z007, 2013Y004),
638 and the Meteorological Special Project of China (GYHY-200906038,
639 GYHY201206037). This paper is partially supported by the CMA Innovation Team
640 for Haze-fog Observation and Forecasts. The authors would also like to thank the
641 LinAn observational station staff for their support. The authors would thank Dr. D.
642 Covert of University of Washington Seattle Department of Atmospheric Sciences
643 USA for useful discussions.

644

645

646 **References**

- 647 Ackerman, A. S., Kirkpatrick, M. P., Stevens, D. E., and Toon, O. B.: The impact of humidity above
648 stratiform clouds on indirect aerosol climate forcing, *Nature*, 432, 1014-1017, 2004.
- 649 Anderson, T., Covert, D., Marshall, S., Laucks, M., Charlson, R., Waggoner, A., Ogren, J., Caldow, R.,
650 Holm, R., and Quant, F.: Performance characteristics of a high-sensitivity, three-wavelength, total
651 scatter/backscatter nephelometer, *J. Atmos. Ocean. Tech.*, 13, 967-986, 1996.
- 652 Anderson, T. L., and Ogren, J. A.: Determining aerosol radiative properties using the TSI 3563
653 integrating nephelometer, *Aerosol Sci. Tech.*, 29, 57-69, 1998.
- 654 Berner, A., Lürzer, C., Pohl, F., Preining, O., and Wagner, P.: The size distribution of the urban aerosol in

655 Vienna, *Sci. Total Environ.*, 13, 245-261, 1979.

656 Birmili, W., Stratmann, F., and Wiedensohler, A.: Design of a DMA-based size spectrometer for a large
657 particle size range and stable operation, *J. Aerosol Sci.*, 30, 549-553, 1999.

658 Carrico, C. M., Rood, M. J., and Ogren, J. A.: Aerosol light scattering properties at Cape Grim, Tasmania,
659 during the first Aerosol Characterization Experiment (ACE 1), *J. Geophys. Res.*, 103, 16565-16574,
660 1998.

661 Carrico, C. M., Rood, M. J., Ogren, J. A., Neusüß, C., Wiedensohler, A., and Heintzenberg, J.: Aerosol
662 Optical properties at Sagres, Portugal during ACE-2, *Tellus B*, 52, 694-715, 2000.

663 Carrico, C. M., Kus, P., Rood, M. J., Quinn, P. K., and Bates, T. S.: Mixtures of pollution, dust, sea salt,
664 and volcanic aerosol during ACE-Asia: Radiative properties as a function of relative humidity, *J.*
665 *Geophys. Res.*, 108, 8650, 10.1029/2003JD003405, 2003.

666 Charlson, R.J., Ahlquist, N., Selvidge, H., and MacCready Jr, P.: Monitoring of atmospheric aerosol
667 parameters with the integrating nephelometer, *JAPCA J. Air Waste Ma.*, 19, 937-942, 1969.

668 Charlson, R. J., Schwartz, S., Hales, J., Cess, R. D., Coakley Jr, J. A., Hansen, J., and Hofmann, D.: Climate
669 forcing by anthropogenic aerosols, *Science*, 255, 423-430, 1992.

670 Cheng, Y., Wiedensohler, A., Eichler, H., Heintzenberg, J., Tesche, M., Ansmann, A., Wendisch, M., Su,
671 H., Althausen, D., and Herrmann, H.: Relative humidity dependence of aerosol optical properties
672 and direct radiative forcing in the surface boundary layer at Xinken in Pearl River Delta of China: An
673 observation based numerical study, *Atmos. Environ.*, 42, 6373-6397, 2008.

674 Chylek, P., and Wong, J.: Effect of absorbing aerosols on global radiation budget, *Geophys. Res. Lett.*,
675 22, 929-931, 1995.

676 Covert, D. S., Charlson, R., and Ahlquist, N.: A study of the relationship of chemical composition and
677 humidity to light scattering by aerosols, *J. Appl. Meteorol.*, 11, 968-976, 1972.

678 Day, D. E., and Malm, W. C.: Aerosol light scattering measurements as a function of relative humidity: a
679 comparison between measurements made at three different sites, *Atmos. Environ.*, 35, 5169-5176,
680 2001.

681 Delene, D. J., and Ogren, J. A.: Variability of aerosol optical properties at four North American surface
682 monitoring sites, *J. Atmos. Sci.*, 59, 1135-1150, 2002.

683 Dick, W. D., Saxena, P., and McMurry, P. H.: Estimation of water uptake by organic compounds in
684 submicron aerosols measured during the Southeastern Aerosol and Visibility Study, *J. Geophys.*
685 *Res.-Atmos.*, 105, 1471-1479, 2000.

686 Doherty, S. J., Quinn, P. K., Jefferson, A., Carrico, C. M., Anderson, T. L., and Hegg, D.: A comparison and
687 summary of aerosol optical properties as observed in situ from aircraft, ship, and land during
688 ACE-Asia, *J. Geophys. Res.*, 110, D04201, doi: 10.1029/2004JD004964, 2005.

689 Engelhart, G., Hildebrandt, L., Kostenidou, E., Mihalopoulos, N., Donahue, N., and Pandis, S.: Water
690 content of aged aerosol, *Atmos. Chem. Phys.*, 11, 911-920, 2011.

691 Fang, S. X., Zhou, L. X., Masarie, K. A., Xu, L., and Rella, C. W.: Study of atmospheric CH₄ mole fractions
692 at three WMO/GAW stations in China, *J. Geophys. Res.-Atmos.*, 118, 4874-4886, 2013.

693 Fierz-Schmidhauser, R., Zieger, P., Gysel, M., Kammermann, L., DeCarlo, P., Baltensperger, U., and
694 Weingartner, E.: Measured and predicted aerosol light scattering enhancement factors at the high
695 alpine site Jungfrauoch, *Atmos. Chem. Phys.*, 10, 2319-2333, 2010.

696 Gasso, S., Hegg, D., Covert, D., Collins, D., Noone, K., Öström, E., Schmid, B., Russell, P., Livingston, J.,
697 and Durkee, P.: Influence of humidity on the aerosol scattering coefficient and its effect on the
698 upwelling radiance during ACE-2, *Tellus B*, 52, 546-567, 2000.

699 Hänel, G.: The properties of atmospheric aerosol particles as functions of the relative humidity at
700 thermodynamic equilibrium with the surrounding moist air, *Adv. Geophys*, 19, 73-188, 1976.

701 Hand, J., and Malm, W.: Review of aerosol mass scattering efficiencies from ground-based
702 measurements since 1990, *J. Geophys. Res.-Atmos.*, 112, D16203, doi:10.1029/2007JD008484,
703 2007.

704 Kim, J., Yoon, S.-C., Jefferson, A., and Kim, S.-W.: Aerosol hygroscopic properties during Asian dust,
705 pollution, and biomass burning episodes at Gosan, Korea in April 2001, *Atmos. Environ.*, 40,
706 1550-1560, 2006.

707 Koloutsou-Vakakis, S., Carrico, C., Kus, P., Rood, M., Li, Z., Shrestha, R., Ogren, J., Chow, J., and Watson,
708 J.: Aerosol properties at a midlatitude Northern Hemisphere continental site, *J. Geophys. Res.*, 106,
709 3019-3032, 2001.

710 Kotchenruther, R. A. and Hobbs, P. V.: Humidification factors of aerosols from biomass burning in
711 Brazil, *J. Geophys. Res.*, 103, 32081-32089, doi: 10.1029/98jd00340, 1998.

712 Kotchenruther, R. A., Hobbs, P. V., and Hegg, D. A.: Humidification factors for atmospheric aerosols off
713 the mid-Atlantic coast of the United States, *J. Geophys. Res.*, 104, 2239-2251, 1999.

714 Li-Jones, X., Maring, H. B., and Prospero, J. M.: Effect of relative humidity on light scattering by mineral
715 dust aerosol as measured in the marine boundary layer over the tropical Atlantic Ocean, *J. Geophys.*
716 *Res.*, 103, 31113-31121, 1998.

717 Liu, X., Zhang, Y., Jung, J., Gu, J., Li, Y., Guo, S., Chang, S.-Y., Yue, D., Lin, P., Kim, Y. J., Hu, M., Zeng, L.,
718 and Zhu, T.: Research on the hygroscopic properties of aerosols by measurement and modeling
719 during CAREBeijing-2006, *J. Geophys. Res.-Atmos.*, 114, D00G16, doi: 10.1029/2008JD010805, 2009.

720 Magi, B. I., and Hobbs, P. V.: Effects of humidity on aerosols in southern Africa during the biomass
721 burning season, *J. Geophys. Res.-Atmos.* 108, 8504, doi:10.1029/2002JD002144, 2003.

722 Malm, W. C., and Day, D. E.: Optical properties of aerosols at Grand Canyon national park, *Atmos.*
723 *Environ.*, 34, 3373-3391, 2000.

724 Malm, W. C., and Day, D. E.: Estimates of aerosol species scattering characteristics as a function of
725 relative humidity, *Atmos. Environ.*, 35, 2845-2860, 2001.

726 Malm, W. C., Day, D. E., Kreidenweis, S. M., Collett, J. L., and Lee, T.: Humidity-dependent optical
727 properties of fine particles during the Big Bend Regional Aerosol and Visibility Observational Study, *J.*
728 *Geophys. Res.*, 108, 4279, doi:10.1029/2002JD002998, 2003.

729 Malm, W. C., Day, D. E., Kreidenweis, S. M., Collett, J. L., Carrico, C., McMeeking, G., and Lee, T.:
730 Hygroscopic properties of an organic-laden aerosol, *Atmos. Environ.*, 39, 4969-4982, 2005.

731 Meng, Z. Y., Jia, X. F., Zhang, R. J., Yu, X. M., and Ma, Q. L.: Characteristics of PM_{2.5} at Lin'an Regional
732 Background Station in the Yangtze River Delta Region, *J. Appl. Meteorol. Sci.*, 23, 424-432, 2012.

733 Morgan, W., Allan, J., Bower, K., Esselborn, M., Harris, B., Henzing, J., Highwood, E., Kiendler-Scharr, A.,
734 McMeeking, G., and Mensah, A.: Enhancement of the aerosol direct radiative effect by
735 semi-volatile aerosol components: airborne measurements in North-Western Europe, *Atmos. Chem.*
736 *Phys.*, 10, 8151-8171, 2010.

737 Müller T., Laborde M., Kassell G., and Wiedensohler A., Design and performance of a three wavelength
738 LED-based total scatter and backscatter integrating nephelometer, *Atmos. Meas. Tech.*, 4(6), 1291-
739 1303, doi:10.5194/amt-4-1291-2011, 2011.

740 Pan, L., Che, H., Geng, F., Xia, X., Wang, Y., Zhu, C., Chen, M., Gao, W., and Guo, J.: Aerosol optical
741 properties based on ground measurements over the Chinese Yangtze Delta Region, *Atmos. Environ.*,
742 44, 2587-2596, 2010.

743 Pan, X. L., Yan, P., Tang, J., Ma, J., Wang, Z., Gbaguidi, A., and Sun, Y.: Observational study of influence
744 of aerosol hygroscopic growth on scattering coefficient over rural area near Beijing mega-city,
745 *Atmos. Chem. Phys.*, 9, 7519-7530, 2009.

746 Pilinis, C., Seinfeld, J. H., and Grosjean, D.: Water content of atmospheric aerosols, *Atmos. Environ.*, 23,
747 1601-1606, 1989.

748 Pilinis, C., Pandis, S. N., and Seinfeld, J. H.: Sensitivity of direct climate forcing by atmospheric aerosols
749 to aerosol size and composition, *J. Geophys. Res.*, 100, 18739-18754, 1995.

750 Qi, H., Lin, W., Xu, X., Yu, X., and Ma, Q.: Significant downward trend of SO₂ observed from 2005 to
751 2010 at a background station in the Yangtze Delta region, China, *Sci. China Ser. B*, 55, 1451-1458,
752 2012.

753 Quinn, P., Marshall, S., Bates, T., Covert, D., and Kapustin, V.: Comparison of measured and calculated
754 aerosol properties relevant to the direct radiative forcing of tropospheric sulfate aerosol on climate,
755 *J. Geophys. Res.*, 100, 8977-8991, 1995.

756 Quinn, P. K., Bates, T. S., Baynard, T., Clarke, A. D., Onasch, T. B., Wang, W., Rood, M. J., Andrews, E.,
757 Allan, J., Carrico, C. M., Coffman, D., and Worsnop, D.: Impact of particulate organic matter on the
758 relative humidity dependence of light scattering: A simplified parameterization, *Geophys. Res. Lett.*,
759 32, L22809, doi: 10.1029/2005gl024322, 2005.

760 Randles, C., Russell, L., and Ramaswamy, V.: Hygroscopic and optical properties of organic sea salt
761 aerosol and consequences for climate forcing, *Geophys. Res. Lett.*, 31, L16108,
762 doi:10.1029/2004GL020628, 2004.

763 Shen, X., Sun, J., Zhang, Y., Wehner, B., Nowak, A., Tuch, T., Zhang, X., Wang, T., Zhou, H., and Zhang, X.:
764 First long-term study of particle number size distributions and new particle formation events of
765 regional aerosol in the North China Plain, *Atmos. Chem. Phys.*, 11, 1565-1580,
766 doi:10.5194/acp-11-1565-2011, 2011.

767 Shi, Y., Chen, J., Hu, D., Wang, L., Yang, X., and Wang, X.: Airborne submicron particulate (PM₁)
768 pollution in Shanghai, China: Chemical variability, formation/dissociation of associated
769 semi-volatile components and the impacts on visibility, *Sci. Total Environ.*, 473, 199-206, 2014.

770 Shi, Z., Zhang, D., Hayashi, M., Ogata, H., Ji, H., and Fujiie, W.: Influences of sulfate and nitrate on the
771 hygroscopic behaviour of coarse dust particles, *Atmos. Environ.*, 42, 822-827, 2008.

772 Sjogren, S., Gysel, M., Weingartner, E., Baltensperger, U., Cubison, M., Coe, H., Zardini, A., Marcolli, C.,
773 Krieger, U., and Peter, T.: Hygroscopic growth and water uptake kinetics of two-phase aerosol
774 particles consisting of ammonium sulfate, adipic and humic acid mixtures, *J. Aerosol Sci.*, 38,
775 157-171, 2007.

776 Sullivan, R., Moore, M., Petters, M., Kreidenweis, S., Roberts, G., and Prather, K.: Effect of chemical
777 mixing state on the hygroscopicity and cloud nucleation properties of calcium mineral dust particles,
778 *Atmos. Chem. Phys.*, 9, 3303-3316, 2009.

779 Sun, J., Zhang, Q., Canagaratna, M. R., Zhang, Y., Ng, N. L., Sun, Y., Jayne, J. T., Zhang, X., Zhang, X., and
780 Worsnop, D. R.: Highly time- and size-resolved characterization of submicron aerosol particles in
781 Beijing using an Aerodyne Aerosol Mass Spectrometer, *Atmos. Environ.*, 44, 131-140, 2010.

782 Sun, Y., Wang, Z., Dong, H., Yang, T., Li, J., Pan, X., Chen, P., and Jayne, J. T.: Characterization of summer
783 organic and inorganic aerosols in Beijing, China with an Aerosol Chemical Speciation Monitor,
784 *Atmos. Environ.*, 51, 250-259, 2012.

785 Tang, I. N.: Chemical and size effects of hygroscopic aerosols on light scattering coefficients, *J. Geophys.*
786 *Res.-Atmos.*, 101, 19245-19250, 1996.

787 Tobo, Y., Zhang, D., Matsuki, A., and Iwasaka, Y.: Asian dust particles converted into aqueous droplets
788 under remote marine atmospheric conditions, *P. Natl. Acad. Sci. USA*, 107, 17905-17910, 2010.

789 Tuch, T. M., Haudek, A., Müller, T., Nowak, A., Wex, H., and Wiedensohler, A.: Design and performance
790 of an automatic regenerating adsorption aerosol dryer for continuous operation at monitoring sites,
791 *Atmos. Meas. Tech.*, 2, 417–422, doi:10.5194/amt-2-417-2009, 2009.

792 Wang, Y., Zhang, X., and Draxler, R. R.: TrajStat: GIS-based software that uses various trajectory
793 statistical analysis methods to identify potential sources from long-term air pollution measurement
794 data, *Environ. Modell. Softw.*, 24, 938–939, 2009.

795 Wang, J. and Martin, S. T.: Satellite characterization of urban aerosols: Importance of including
796 hygroscopicity and mixing state in the retrieval algorithms, *J. Geophys. Res.-Atmos.*, 112, D17203,
797 doi:10.1029/2006JD008078, 2007.

798 Wang, M. X., Ding, X., Fu, X., He, Q., Wang, S., Bernard, F., Zhao, X., and Wu, D.: Aerosol scattering
799 coefficients and major chemical compositions of fine particles observed at a rural site in the central
800 Pearl River Delta, South China, *J. Environ. Sci.*, 24, 72–77, 2012.

801 Wang, L. P., Zhang, B. H., and Zhang, X. W.: Main weather processes in March and April, 2013, *Weather
802 Forecast Rev.*, 5, 1–7, 2013.

803 Weingartner, E., Baltensperger, U., and Burtscher, H.: Growth and structural change of combustion
804 aerosols at high relative humidity, *Environ. Sci. Technol.*, 29, 2982-2986, 1995.

805 Wiscombe, W., and Grams, G.: The backscattered fraction in two-stream approximations, *J. Atmos. Sci.*,
806 33, 2440-2451, 1976.

807 Xu, J., Bergin, M., Yu, X., Liu, G., Zhao, J., Carrico, C., and Baumann, K.: Measurement of aerosol
808 chemical, physical and radiative properties in the Yangtze delta region of China, *Atmos. Environ.*, 36,
809 161-173, 2002.

810 Xu, X., Lin, W., Wang, T., Yan, P., Tang, J., Meng, Z., and Wang, Y.: Long-term trend of surface ozone at a
811 regional background station in eastern China 1991–2006: enhanced variability, *Atmos. Chem. Phys.*,
812 8, 2595-2607, doi:10.5194/acp-8-2595-2008, 2008.

813 Yan, P., Zhang, Y. M., Yang, D. Z., Tang, J., Yu, X. L., Cheng, H. B., and Yu, X. M.: The characteristic of
814 aerosol ionic size distributions at Lin'an in summer of 2003, *Acta Meteor. Sin.*, 63, 980–987, 2005.

815 Yan, P., Pan, X., Tang, J., Zhou, X., Zhang, R., and Zeng, L.: Hygroscopic growth of aerosol scattering
816 coefficient: A comparative analysis between urban and suburban sites at winter in Beijing,
817 *Particuology*, 7, 52-60, 2009.

818 Zhang, B. and Sun, J.: Analysis of the March 2013 atmospheric circulation and Weather, *Meteor. Mon.*,
819 39, 794–800, 2013.

820 Zhang, Y. Y., Zuo, L. F., Ren, X. C., and Cui, J.: Research of the aerosol scattering properties based on
821 evaporation duct, *Ship Electron. Eng.*, 32, 12–14, 2012.

822 Zhejiang Environmental Protection Bureau (ZEPB), 1999, Annual Report on the State of the
823 Environment of Zhejiang Province, Zhejiang Environmental Protection Bureau, Hangzhou, 1999.

824 Zhejiang Environmental Protection Bureau (ZEPB), 2006, Annual Report on the State of the
825 Environment of Zhejiang Province, Zhejiang Environmental Protection Bureau, Hangzhou, 21 pp.,
826 2006.

827 Zhejiang Environmental Protection Bureau (ZEPB), 2012, Annual Report on the State of the
828 Environment of Zhejiang Province, Zhejiang Environmental Protection Bureau, Hangzhou, 29 pp.,
829 2012.

830 Zhejiang Environmental Protection Bureau (ZEPB), 2013, Annual Report on the State of the

831 Environment of Zhejiang Province, Zhejiang Environmental Protection Bureau, Hangzhou, 33 pp.,
 832 2013.

833 Zieger, P., Fierz-Schmidhauser, R., Gysel, M., Ström, J., Henne, S., Yttri, K. E., Baltensperger, U., and
 834 Weingartner, E.: Effects of relative humidity on aerosol light scattering in the Arctic, *Atmos. Chem.*
 835 *Phys.*, 10, 3875-3890, doi:10.5194/acp-10-3875-2010, 2010.

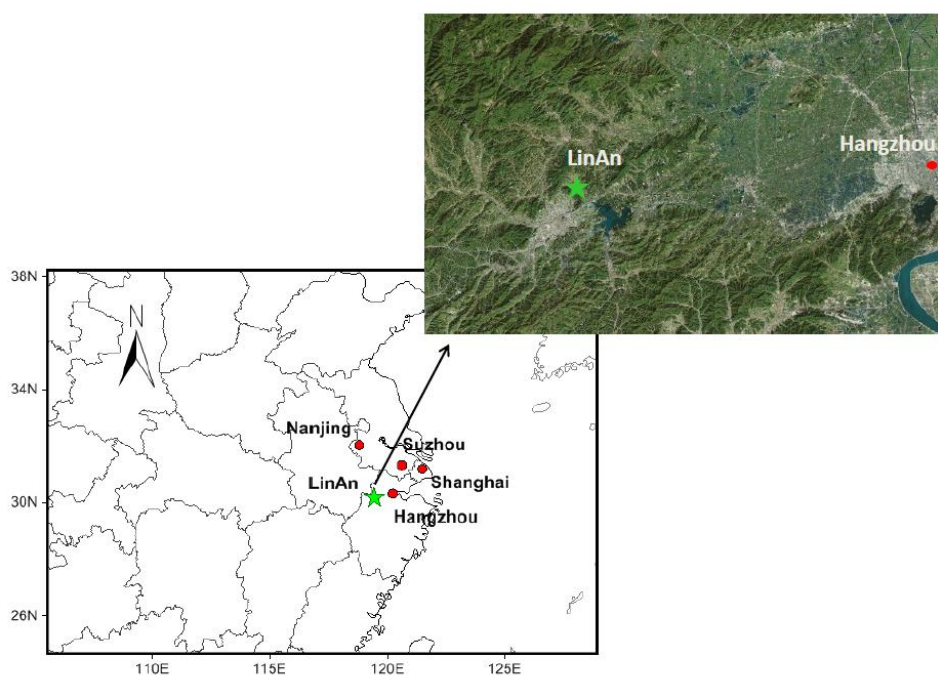
836 Zieger, P., Weingartner, E., Henzing, J., Moerman, M., Leeuw, G. d., Mikkilä, J., Ehn, M., Petäjä, T.,
 837 Clémer, K., and Roozendaal, M. v.: Comparison of ambient aerosol extinction coefficients obtained
 838 from in-situ, MAX-DOAS and LIDAR measurements at Cabauw, *Atmos. Chem. Phys.*, 11, 2603-2624,
 839 doi:10.5194/acp-11-2603-2011, 2011.

840 Zieger, P., Kienast-Sjögren, E., Starace, M., Bismarck, J. v., Bukowiecki, N., Baltensperger, U., Wienhold,
 841 F., Peter, T., Ruhtz, T., and Collaud Coen, M.: Spatial variation of aerosol optical properties around
 842 the high-alpine site Jungfraujoch (3580 m asl), *Atmos. Chem. Phys.*, 12, 7231-7249,
 843 doi:10.5194/acp-12-7231-2012, 2012.

844 Zieger, P., Fierz-Schmidhauser, R., Weingartner, E., and Baltensperger, U.: Effects of relative humidity
 845 on aerosol light scattering: results from different European sites, *Atmos. Chem. Phys.*, 13,
 846 10609-10631, doi:10.5194/acp-13-10609-2013, 2013.

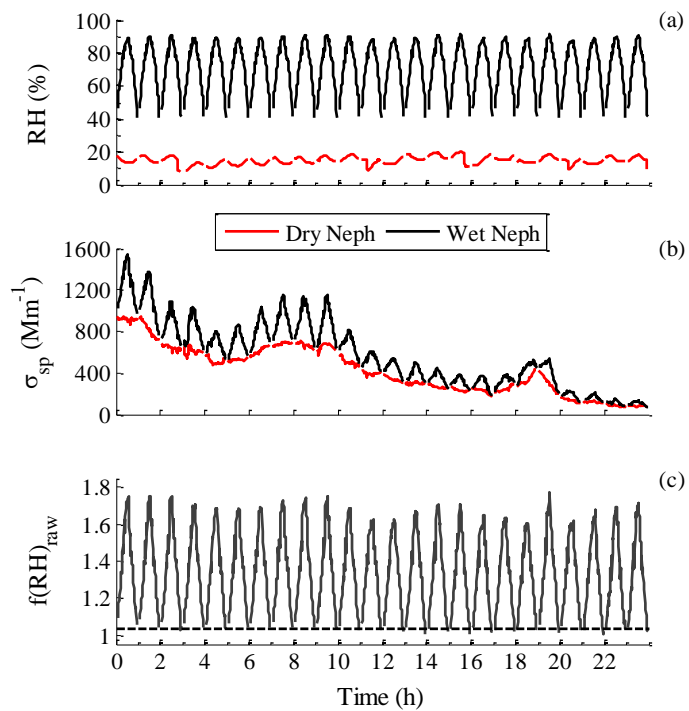
847 Zieger, P., Fierz-Schmidhauser, R., Poulain, L., Müller, T., Birmili, W., Spindler, G., Wiedensohler, A.,
 848 Baltensperger, U., and Weingartner, E.: Influence of water uptake on the aerosol particle light
 849 scattering coefficients of the Central European aerosol, *Tellus B*, 66, 22716,
 850 doi:10.3402/tellusb.v66.22716, 2014.

851



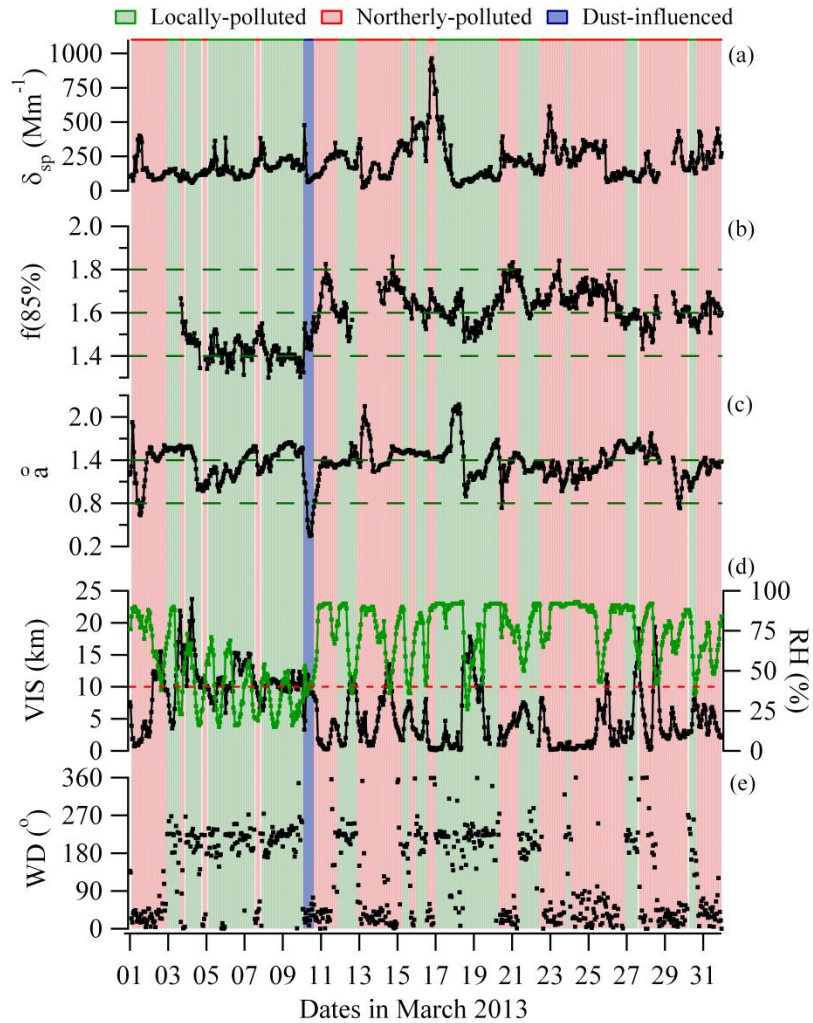
852

853 Fig. 1 Location of LinAn station (green star) and the main cities in the Yangtze River
 854 Delta (red dots) in the lower left panel. The upper right panel shows the topography of
 855 the surrounding area.



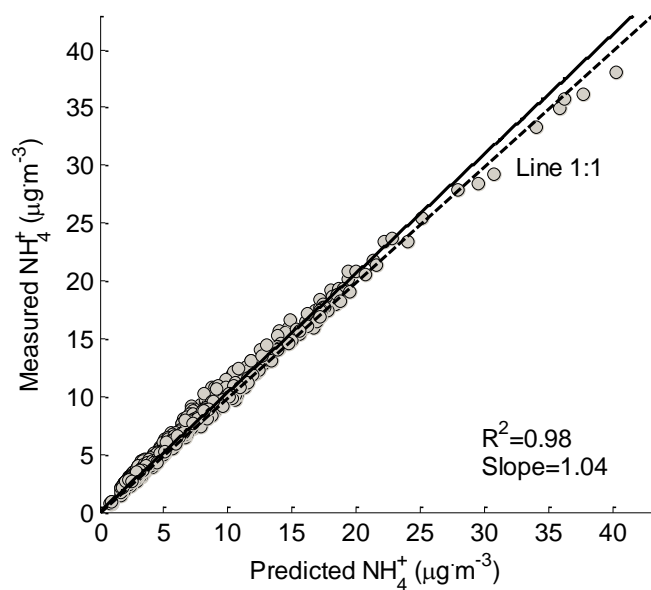
856

857 Fig. 2 Example of measured data on 17 March 2013 (a) Relative humidity inside
 858 DryNeph (red line) and WetNeph (black line); (b) Aerosol scattering coefficients
 859 measured by DryNeph (red line) and WetNeph (black line) at 550nm wavelength; (c)
 860 Raw scattering enhancement factor $f(\text{RH}, 550\text{nm})_{\text{raw}}$ without normalization, the black
 861 dashed line is at $f(\text{RH})_{\text{raw}}=1.03$.



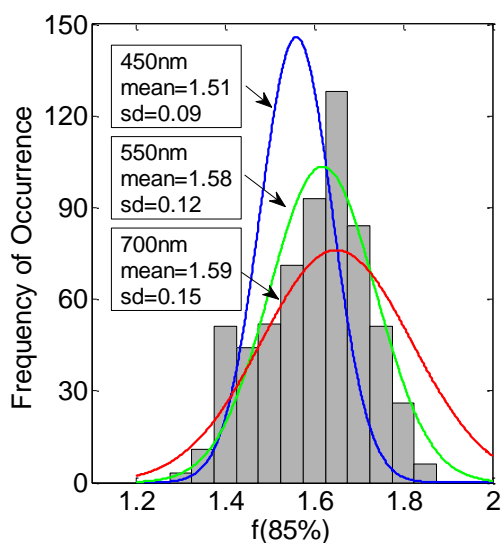
862

863 Fig. 3 Time series of measured and derived aerosol variables, as well as the ambient
 864 RH and visibility. (a) Aerosol scattering coefficient of DryNeph at 550 nm
 865 wavelength; (b) scattering enhancement factor $f(85\%)$ at 550 nm wavelength; (c)
 866 Ångström exponent α_{a} (d) visibility (VIS) and relative humidity (RH) at ambient
 867 conditions, the red dashed line represents $\text{VIS}=10$ km; (e) wind direction (WD),
 868 indicating that prevailing wind directions during the observation period were mainly
 869 northeasterly (NE) and southwesterly (SW).



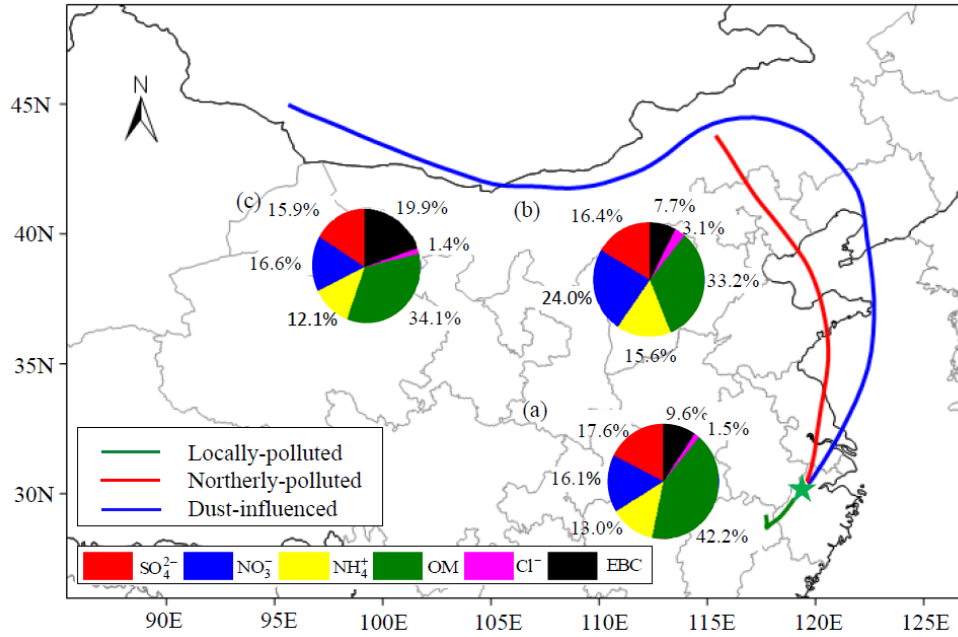
870

871 Fig. 4 Measured and predicted mass concentration of ammonium. The predicted mass
 872 concentration of ammonium (NH_4^+ predicted) is calculated by Eq. (4). The solid black
 873 line represents the linear least square regression.



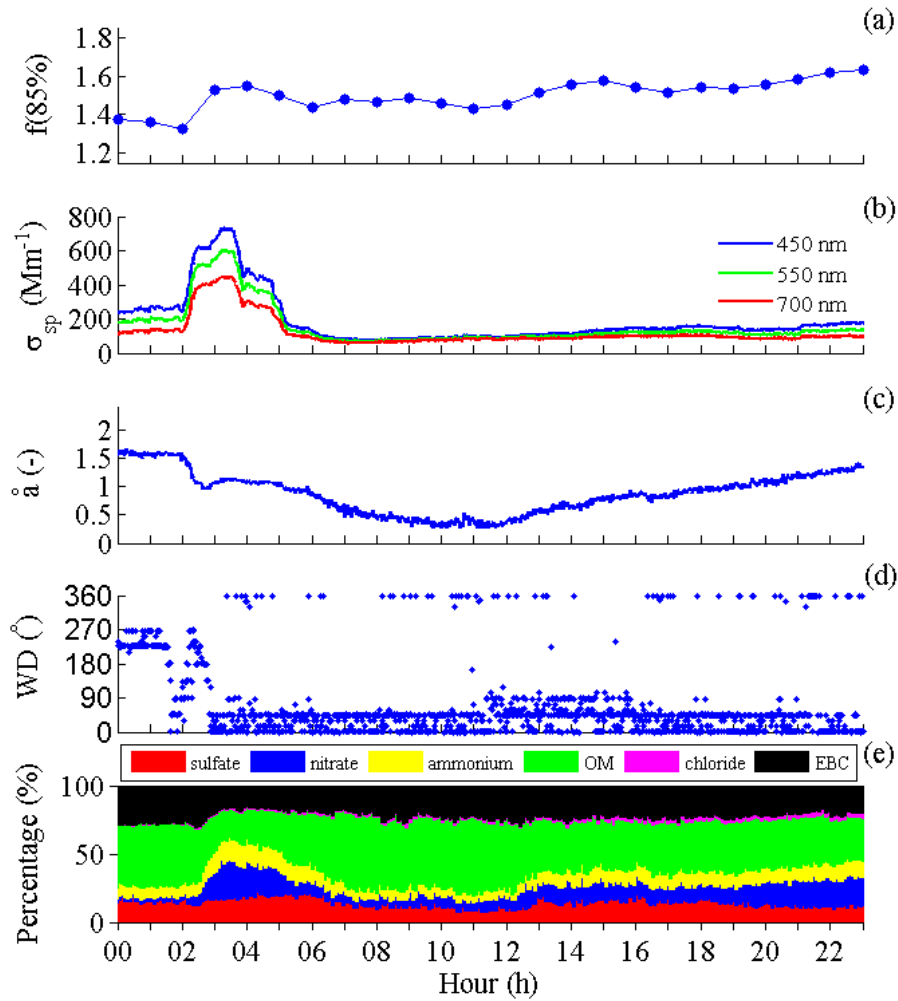
874

875 Fig. 5 Histogram of $f(85\%, 550 \text{ nm})$ overlaid with the Gaussian curves based on the
 876 statistics for $f(85\%, 450 \text{ nm})$, $f(85\%, 550 \text{ nm})$ and $f(85\%, 700 \text{ nm})$.



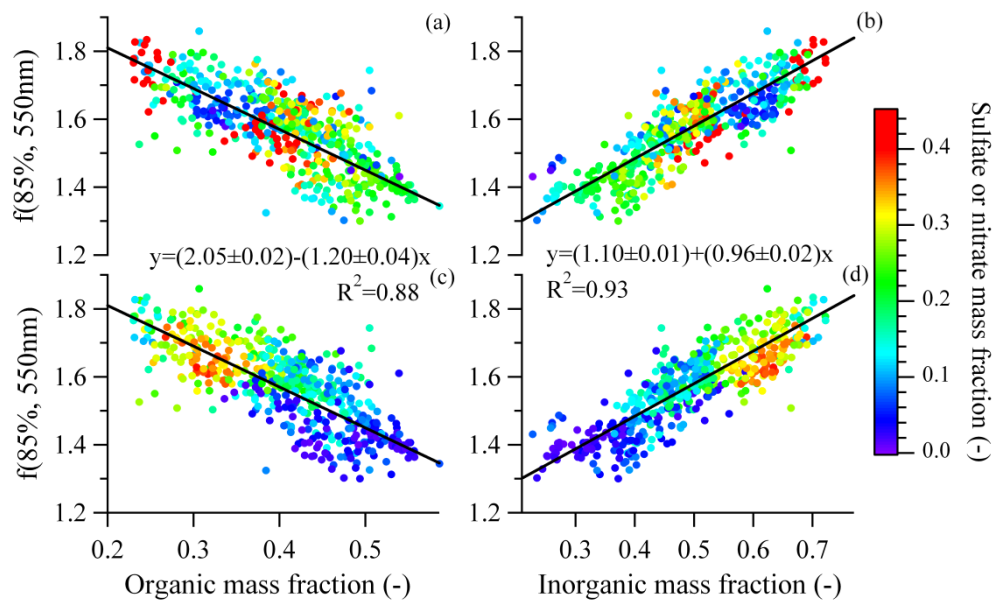
877

878 Fig. 6 72h back trajectories of locally-polluted periods, northerly-polluted periods and
 879 dust-influenced period, together with the mean mass fractions of submicron chemical
 880 species (SO₄²⁻, NO₃⁻, NH₄⁺, OM and Cl⁻) measured by AMS and EBC in PM₁₀
 881 measured by MAAP. The pie charts (a), (b) and (c) were for locally-polluted,
 882 northerly-polluted and dust-influenced periods, respectively.



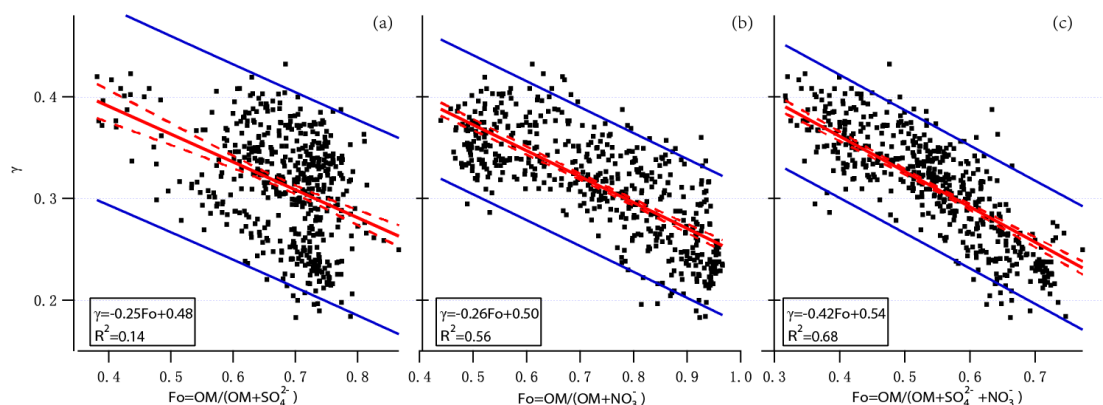
883

884 Fig. 7 Parameters in episode influenced by dust on 10 March 2013 at LinAn (a)
 885 scattering enhancement factor $f(85\%)$ at 550nm wavelength; (b) scattering
 886 coefficients at 450nm, 550nm and 700nm wavelengths; (c) Ångström exponent \tilde{a} (d)
 887 wind direction; (e) mass percentages of chemical species measured by AMS and
 888 MAAP.



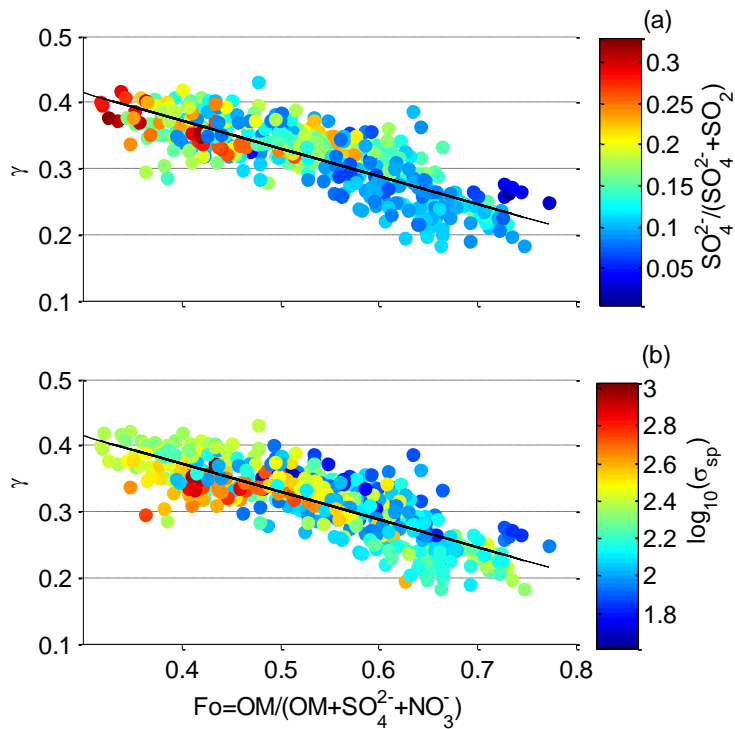
889

890 Fig. 8 Scattering enhancement factor $f(85\%, 550\text{nm})$ vs. organic mass fraction and
 891 inorganic mass fraction determined from AMS and MAAP: (a) (b) $f(85\%, 550\text{nm})$ vs.
 892 organic mass and inorganic mass fraction colored by sulfate mass fraction; (c) (d)
 893 $f(85\%, 550\text{nm})$ vs. organic mass fraction and inorganic mass fraction colored by
 894 nitrate mass fraction. The solid black line represent a bivariate linear regression
 895 including the uncertainty of $f(85\%, 550\text{nm})$ and the standard deviation of chemical
 896 compositions.



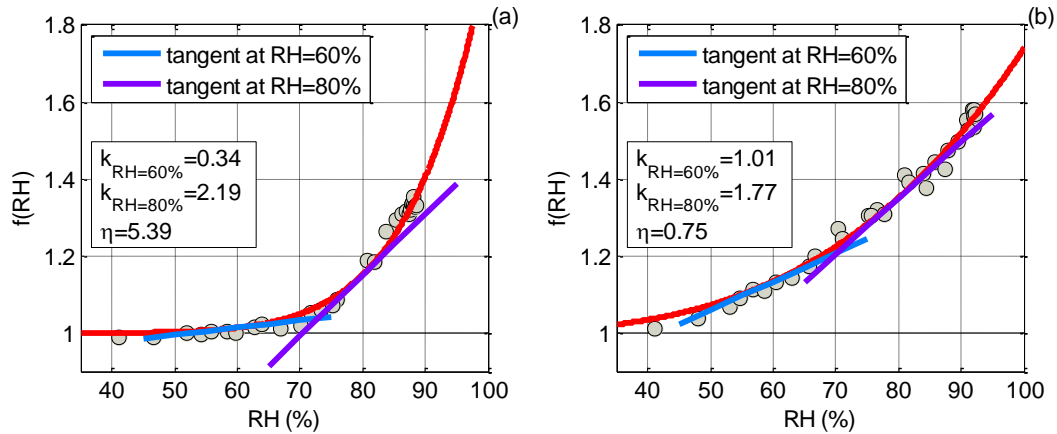
897

898 Fig. 9 scatter plots of γ versus F_o (a) $F_o = \text{OM} / (\text{OM} + \text{SO}_4^{2-})$, (b) $F_o = \text{OM} / (\text{OM} + \text{NO}_3^-)$
 899 and (c) $F_o = \text{OM} / (\text{OM} + \text{SO}_4^{2-} + \text{NO}_3^-)$. Solid red lines represent the linear fit, dashed red
 900 lines show the 95% confidence level for the fit, and solid blue lines show the 95%
 901 prediction bands.



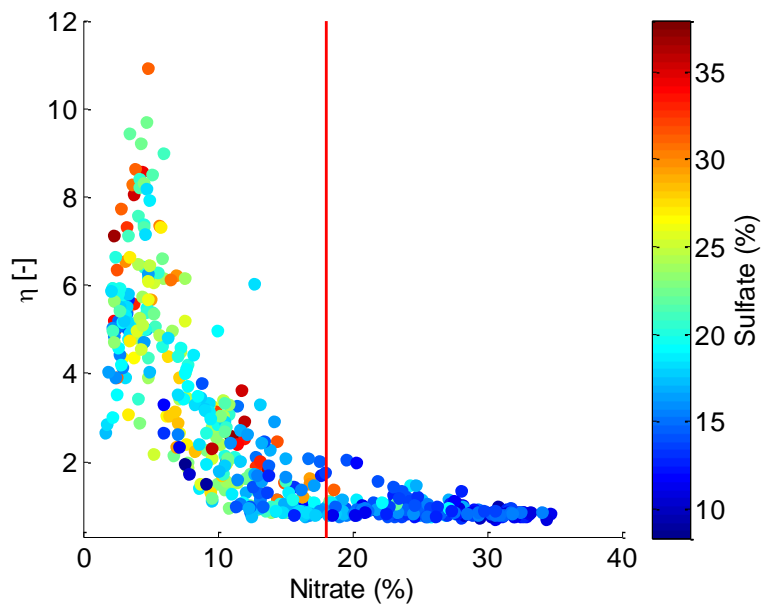
902

903 Fig. 10 γ versus $Fo=OM/(OM+SO_4^{2-}+NO_3^-)$ colored by (a) $SO_4^{2-}/(SO_4^{2-}+SO_2)$ molar
 904 ratio and (b) $\log_{10}(\sigma_{sp})$.



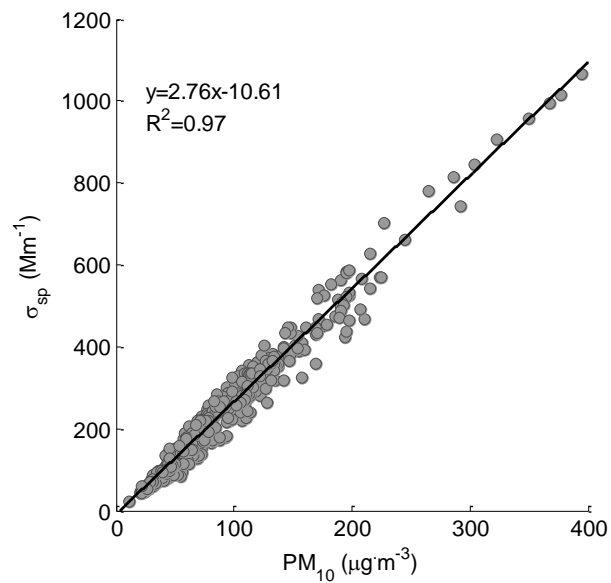
905

906 Fig. 11 Two distinct examples showing different growth patterns and the
 907 corresponding η (a) 2013.03.08 18h $f(RH)$ increased slowly at low RH (usually <70%)
 908 and then increase more steeply, thus η is big; (b) 2013.03.10 21h $f(RH)$ increased at a
 909 nearly constant rate and η is small. $k_{RH=60\%}$ and $k_{RH=80\%}$ represent the derivatives at 60%
 910 and 80% RH, respectively. $f(RH)$ given at 550nm wavelength.



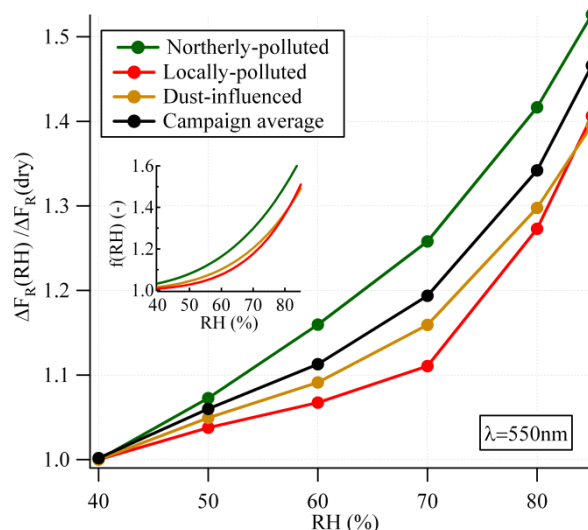
911

912 Fig. 12 Scatter plot of η and the mass percentage of nitrate, colored by the mass
 913 percentage of sulfate.



914

915 Fig. 13 Linear regression of scattering coefficients (σ_{sp}) at 550nm wavelength and
 916 PM_{10} mass concentration.



917

918 Fig. 14 Influence of relative humidity (RH) on direct radiative forcing for the entire
 919 campaign (black line), as well as for the northerly-polluted, locally-polluted and
 920 dust-polluted periods, measured by the ratio of radiative forcing at a certain RH to
 921 that at dry conditions. The small inlay shows the fitting curves of $f(\text{RH})$ for
 922 northerly-polluted, locally-polluted and dust-polluted periods, respectively, using
 923 fitting parameters in Table 6. All the parameters were measured at 550nm wavelength.

924

925 Table 1 Averaged enhancement factors and mean standard deviations for scattering
 926 coefficient, backscattering coefficient and hemispheric backscatter fraction at
 927 different RHs (550nm wavelength).

RH(%)	$f(\text{RH})$	$f_b(\text{RH})$	$f_\beta(\text{RH})$
50	1.07(0.04)	1.04(0.02)	0.96(0.02)
60	1.14(0.08)	1.06(0.04)	0.93(0.04)
70	1.24(0.11)	1.10(0.05)	0.89(0.05)
80	1.43(0.12)	1.18(0.07)	0.83(0.05)
85	1.58(0.12)	1.25(0.07)	0.79(0.04)

928

929 Table 2 Summary of mass concentrations ($\mu\text{g}\cdot\text{m}^{-3}$) of aerosol species measured by
 930 AMS as well as MAAP(*) (SD: standard deviation)

Mean	SD	Minimum	Maximum
------	----	---------	---------

Sulfate	8.1	4.1	0.1	26.1
Nitrate	9.8	12.1	0.2	79.2
Ammonium	6.9	5.5	0.5	42.8
Chloride	1.1	2.0	0.002	22.9
OM	17.7	11.1	2.8	93.9
EBC*	4.1	2.8	0.7	25.3

931 * EBC was measured by MAAP in PM₁₀.

932

933 Table 3 Statistical values of f(85%) at 450 nm, 550 nm and 700 nm wavelengths (SD:
934 standard deviation; prctl: percentile)

λ	mean	SD	90th prctl.	75th prctl.	median	25th prctl.	10th prctl.
450 nm	1.51	0.09	1.63	1.58	1.53	1.47	1.39
550 nm	1.58	0.12	1.72	1.65	1.59	1.49	1.40
700 nm	1.59	0.15	1.77	1.70	1.62	1.46	1.36

935

936 Table 4 Average enhancement factors and mean standard deviations for scattering
937 coefficient, backscattering coefficient and hemispheric backscatter fraction in various
938 observation episodes (550nm wavelength).

	Locally-polluted	Northerly-polluted	Dust-influenced
f(80%)	1.36(0.11)	1.50(0.09)	1.37(0.05)
f _b (80%)	1.15(0.06)	1.21(0.06)	1.15(0.03)
f _{β} (80%)	0.85(0.04)	0.81(0.03)	0.84(0.03)
f(85%)	1.52(0.10)	1.64(0.09)	1.48(0.05)
f _b (85%)	1.21(0.06)	1.28(0.06)	1.19(0.04)
f _{β} (85%)	0.80(0.02)	0.78(0.02)	0.81(0.03)
N	295	303	14

939

940 Table 5 Curve-fitting parameters of f(RH) at 550nm wavelength for various aerosol
941 types using equation $f(\text{RH})=c (1-\text{RH})^g$.

c	g	Reference
---	---	-----------

Locally-polluted	0.85±0.08	0.29±0.04	
Northerly-polluted	0.93±0.07	0.28±0.03	This work
Dust-influenced	0.87±0.05	0.27±0.02	
Continental	0.9	0.59	Zieger et al. (2014)
Arctic ^a	1	0.58±0.09	Zieger et al. (2010)
Marine	0.99	0.54	
Polluted	0.59	0.77	Carrico et al. (2003)
Dust	0.60	0.61	
Polluted Marine	1	0.57±0.06	
Dust	1	0.23±0.05	Gass ó et al. (2000)
Clean Marine1 ^b	1	0.69±0.06	
Clean Marine2 ^c	1	0.73±0.07	

942 a fitting results for aerosol samples with RH>75%

943 b fitting results for aerosol samples with RH>60%

944 c fitting results for aerosol samples with RH>80%

945

946 Table 6 Curve-fitting parameters of f(RH) at 550nm wavelength for various aerosol

947 types in terms of Eq. (5).

	a	b	Reference
Locally-polluted	1.24±0.29	5.46±1.90	
Northerly-polluted	1.20±0.21	3.90±1.27	This work
Dust-influenced	1.02±0.19	4.51±0.80	
Clean	1.20±0.06	6.07±0.27	
Polluted	2.30±0.03	6.27±0.10	Pan et al. (2009)
Dust	0.64±0.04	5.17±0.40	
Urban	2.06	3.60	
Mixed	3.26	3.85	Liu et al. (2007)
Marine	4.92	5.04	

948

949 Table 7 Estimated effects of aerosol hygroscopic growth on direct radiative forcing by
 950 locally-polluted, northerly-polluted and dust-influenced aerosols at LinAn, measured
 951 by the ratio ($\Delta F_R(\text{RH}_{\text{amb}})/\Delta F_R(\text{dry})$) of direct aerosol radiative forcing at the ambient
 952 average relative humidity ($\text{RH}_{\text{amb}}=67\%$) for the entire campaign to that in dry
 953 condition. All the parameters were measured at 550nm wavelength.

	$f(\text{RH}_{\text{amb}})$	$b(\text{dry})$	$\bar{\beta}(\text{dry})$	$b(\text{RH}_{\text{amb}})$	$\bar{\beta}(\text{RH}_{\text{amb}})$	$\Delta F_R(\text{RH}_{\text{amb}})/\Delta F_R(\text{dry})$
Entire campaign	1.21	0.126	0.268	0.115	0.255	1.157
Locally-polluted	1.17	0.131	0.274	0.123	0.263	1.118
Northerly-polluted	1.26	0.121	0.262	0.106	0.243	1.195
Dust-influenced	1.15	0.146	0.289	0.132	0.274	1.105

954